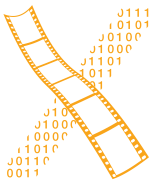

Chair for Computer Science 10 (Media Computing and Human-Computer Interaction)

RWTH AACHEN UNIVERSITY

Designing a Magnetic Field Sensor Grid for 2D Mid-Air Gesture Recognition

Bachelor's Thesis
submitted to the
Media Computing Group
Prof. Dr. Jan Borchers
Computer Science Department
RWTH Aachen University

by
Laura Drescher-Manaa

Thesis advisor:
Prof. Dr. Jan Borchers

Second examiner:
Prof. Dr. Jürgen Steimle

Registration date: 06.05.2022
Submission date: 05.09.2022

Zentrales Prüfungsamt/Central Examination Office

Eidesstattliche Versicherung
Statutory Declaration in Lieu of an Oath

Name, Vorname/Last Name, First Name

Matrikelnummer (freiwillige Angabe)
Matriculation No. (optional)

Ich versichere hiermit an Eides Statt, dass ich die vorliegende Arbeit/Bachelorarbeit/ Masterarbeit* mit dem Titel
I hereby declare in lieu of an oath that I have completed the present paper/Bachelor thesis/Master thesis* entitled

selbstständig und ohne unzulässige fremde Hilfe (insbes. akademisches Ghostwriting) erbracht habe. Ich habe keine anderen als die angegebenen Quellen und Hilfsmittel benutzt. Für den Fall, dass die Arbeit zusätzlich auf einem Datenträger eingereicht wird, erkläre ich, dass die schriftliche und die elektronische Form vollständig übereinstimmen. Die Arbeit hat in gleicher oder ähnlicher Form noch keiner Prüfungsbehörde vorgelegen.
independently and without illegitimate assistance from third parties (such as academic ghostwriters). I have used no other than the specified sources and aids. In case that the thesis is additionally submitted in an electronic format, I declare that the written and electronic versions are fully identical. The thesis has not been submitted to any examination body in this, or similar, form.

Ort, Datum/City, Date

Unterschrift/Signature

*Nichtzutreffendes bitte streichen

*Please delete as appropriate

Belehrung:
Official Notification:

§ 156 StGB: Falsche Versicherung an Eides Statt
Wer vor einer zur Abnahme einer Versicherung an Eides Statt zuständigen Behörde eine solche Versicherung falsch abgibt oder unter Berufung auf eine solche Versicherung falsch aussagt, wird mit Freiheitsstrafe bis zu drei Jahren oder mit Geldstrafe bestraft.
Para. 156 StGB (German Criminal Code): False Statutory Declarations
Whoever before a public authority competent to administer statutory declarations falsely makes such a declaration or falsely testifies while referring to such a declaration shall be liable to imprisonment not exceeding three years or a fine.
§ 161 StGB: Fahrlässiger Falscheid; fahrlässige falsche Versicherung an Eides Statt
(1) Wenn eine der in den §§ 154 bis 156 bezeichneten Handlungen aus Fahrlässigkeit begangen worden ist, so tritt Freiheitsstrafe bis zu einem Jahr oder Geldstrafe ein.
(2) Straflosigkeit tritt ein, wenn der Täter die falsche Angabe rechtzeitig berichtigt. Die Vorschriften des § 158 Abs. 2 und 3 gelten entsprechend.
Para. 161 StGB (German Criminal Code): False Statutory Declarations Due to Negligence
(1) If a person commits one of the offences listed in sections 154 through 156 negligently the penalty shall be imprisonment not exceeding one year or a fine.
(2) The offender shall be exempt from liability if he or she corrects their false testimony in time. The provisions of section 158 (2) and (3) shall apply accordingly.

Die vorstehende Belehrung habe ich zur Kenntnis genommen:
I have read and understood the above official notification:

Ort, Datum/City, Date

Unterschrift/Signature

Contents

List of Figures

List of Tables

Abstract

Since gestures are a natural form of human communication, gesture recognition is a widely used method of user input in the field of human-computer interaction. While smartphones are operated almost exclusively by gestures, this is not the case for other devices in daily use such as computers or televisions. However, previous approaches to gesture recognition are too inconvenient to replace devices such as keyboards or remote controls. Therefore, we propose a magnetic field sensor grid that is suitable for 2D mid-air gesture recognition and a convenient embedding into people's homes. Based on four AMR sensors, a ∅8mmx2mm disk magnet, and a linear weighting algorithm, our system allows for a reliable user input height of 15-20cm, an adjustable sensor spacing, and an expandable sensing area.

In this thesis, we set concrete requirements for our system and pick an AMR sensor that is able to fulfill them. We construct a modular sensor adapter PCB and implement the control and calibration of the sensor with an Arduino. We examine the sensor and the magnetic field progression of several magnets to find one that is suitable for mid-air interaction. After choosing the magnet, we evaluate the suitability of our setup for 2D mid-air gesture recognition by applying two position estimation approaches that are based on linear weighting. Thereby, the first approach directly applies linear weighting, while the second approach linearizes the magnetic field measurements beforehand. The results show that the second approach performs best around 10cm sensor spacing.

Überblick

Da Gesten eine natürliche Form der menschlichen Kommunikation sind, ist Gestenerkennung eine weit verbreitete Methode der Benutzereingabe im Bereich der Mensch-Computer-Interaktion. Während Smartphones fast ausschließlich durch Gesten bedient werden, ist dies bei anderen Geräten des täglichen Gebrauchs wie Computern oder Fernsehern nicht der Fall. Bisherige Ansätze zur Gestenerkennung sind jedoch zu umständlich, um Geräte wie Tastaturen oder Fernbedienungen zu ersetzen. Daher schlagen wir ein Magnetfeldsensornetz vor, das für die 2D Gestenerkennung in der Luft geeignet ist und sich in Wohnungen einbauen lässt ohne die Bewohner zu stören. Basierend auf vier AMR-Sensoren, einem ∅8mmx2mm Scheibenmagneten und einem linearen Gewichtungsalgorithmus ermöglicht unser System eine zuverlässige Benutzereingabehöhe von 15-20cm, einen einstellbaren Sensorabstand und einen erweiterbaren Erfassungsbereich.

In dieser Arbeit stellen wir konkrete Anforderungen an unser System und wählen einen AMR-Sensor aus, der diese erfüllen kann. Wir konstruieren eine modulare Sensoradapterplatine und implementieren die Steuerung und Kalibrierung des Sensors mit einem Arduino. Wir untersuchen den Sensor und den Magnetfeldverlauf mehrerer Magnete, um einen zu finden, der für die Interaktion in der Luft geeignet ist. Nach der Auswahl des Magneten evaluieren wir die Eignung unseres Aufbaus für die 2D Gestenerkennung in der Luft, indem wir zwei Positionsschätzungsansätze anwenden, die auf linearer Gewichtung beruhen. Dabei wendet der erste Ansatz direkt eine lineare Gewichtung an, während der zweite Ansatz die Magnetfeldmessungen vorher linearisiert. Die Ergebnisse zeigen, dass der zweite Ansatz bei einem Sensorabstand um die 10cm am besten abschneidet.

Acknowledgements

Firstly, I would like to thank Prof. Dr. Jan Borchers and Prof. Dr. Jürgen Steimle for examining this bachelor thesis.

Secondly, I want to thank my supervisors René Schäfer and Martin Schmitz for their advice, feedback and time throughout my thesis.

Lastly, I would like to thank my family and friends for their support. Especially, I want to thank Dustin Schneider, Fredrik Konrad, Valentino Geuenich, Lukas Johanns and Dominik Wirtz for their advice.

Conventions

Throughout this thesis we use the following conventions.

Text conventions

Definitions of technical terms or short excursus are set off in coloured boxes.

EXCURSUS:
Excursus are detailed discussions of a particular point in a book, usually in an appendix, or digressions in a written text.

Definition:
Excursus

The whole thesis is written in American English. The first person is written in plural form and unidentified third persons are referred to in male form.

Download links are set off in coloured boxes.

File: myFile

Chapter 1

Introduction

Gestures are a natural form of human communication. Therefore, the use of gestures has been extended to human-computer interaction for commonly used devices like smartphones and tablets. Gestures are widely accepted as user input method for smartphones, which suggests the expansion to further devices like computers and televisions. There are various approaches to gesture recognition, including approaches based on mechanomyograms sensors [Yamakawa and Nojima, 2012], Electrical Impedance Tomography [Zhang et al., 2016], infrared signals [Gong et al., 2017], [Ogata et al., 2012], cameras [Chan et al., 2015] and magnetic field sensors [Chan et al., 2013], [Chen et al., 2013], [Chen et al., 2016].

Gesture recognition could be used as a user input method for devices like computers and televisions.

While these are promising approaches, they are either inconvenient to wear, limited in their gesture spectrum, restrain the user from pursuing everyday activities due to their construction or not socially acceptable in respect to their appearance. Furthermore, all these approaches are hand-held and meant for mobile applications, so when using one to operate the television, it would occupy space in its vicinity during the time the television is not used, which could be inconvenient to the user.

Previous gesture recognition approaches are too inconvenient for integration into people's homes.

Instead, an embedded approach for gesture recognition might be more favorable that uses unused spaces, like the bottom of a tabletop. Such an approach can always stay

A magnetic field sensor grid could be used as a convenient user input device.

connected to the device and is always ready to use. Since the approach is embedded, it is invisible to the user and is therefore no inconvenience in terms of its appearance or spatial requirements. In turn, it needs to be able to recognize gestures through surfaces of varying materials. The pioneering approach GaussSense Liang et al. [2012] embedded a magnetic field sensor grid into the back of a device in order to extend the device's functionality by using a stylus. Similarly, we can embed such a sensor grid under a tabletop while interacting with the sensor grid from above the table via a magnet.

Previous approaches, that are based on magnetic field sensor grids, do not support a large enough input distance for gestural input.

However, while there are many approaches that use magnetic field sensor grids Liang et al. [2015], Chan et al. [2013], Gu et al. [2019], Liang et al. [2013], Chen et al. [2013], they are too large to be embedded into an object or their sensing distance is restricted to under 5cm, which is likely not large enough for a user to perform a gesture without issues. By extending the sensing distance to mid-air, gestural input is possible. In addition, a clean sensing area on the table is not necessary, which enhances user comfort.

With this reasoning, we construct a sensor grid that is suitable for 2D mid-air gesture recognition in this thesis.

1.1 Outline

Chapter 2 covers the background needed to understand some aspects of this thesis. In Chapter 3, we discuss recent work in the fields of magnetic tracking and gesture recognition.

We describe the requirements for our system in Chapter 4. Based on that, we choose a suitable magnetic field sensor and construct a modular sensor adapter PCB in Chapter 5. In Chapter 6, we conduct experiments with various magnets to find a magnet that meets the requirements.

In order to evaluate the suitability of the sensor-magnet combination for 2D mid-air gesture recognition, we apply two 2D position estimation approaches in Chapter 7 at

varying sensor spacings and magnet heights. In Chapter 8, we discuss the evaluation results, check the requirements and compare our setup to other approaches.

Lastly, we summarize the contents of this thesis and give an outline for future work in Chapter 9.

Chapter 2

Background

In this chapter, we discuss basic concepts and laws concerning magnetic fields. Further, we introduce the *magnetic field space* by Chen et al. [2013].

2.1 The Magnetic Field, The B-field and Units

A magnetic field is a vector field and is measured in tesla or gauss.

A permanent magnet is surrounded by a magnetic field, where the directed magnetic field lines run from the north pole to the south pole. The magnetic field can be described by the magnetic flux density, which is often called **B**-field. The **B**-field is a vector field that assigns a vector **B** to each point p in space, where **B** describes the direction and strength of the magnetic field at p (See Figure 2.1)). The SI unit of **B** is tesla (T) and the Gaussian unit is gauss (G), where gauss and tesla are proportional with 1T $\widehat{=}$ 10000G. Both units are commonly used.

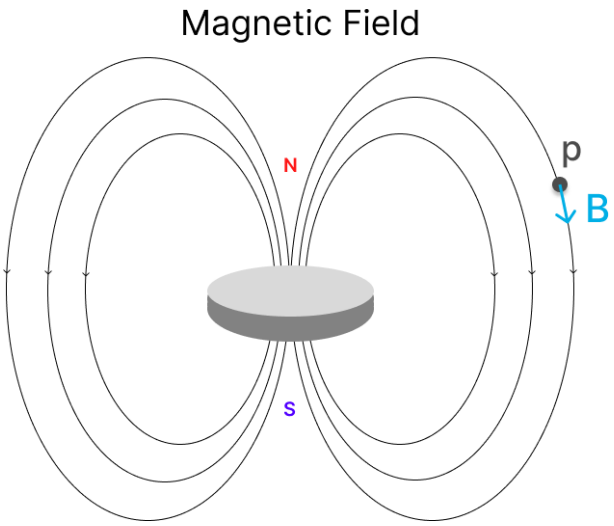

Figure 2.1: A visualization of a magnetic field, induced by a magnet, with the magnetic field lines running from the north pole to the south pole. The B-field assigns a vector **B** to each point p in space in order to describe the direction and the strength of the magnetic field at p.

2.2 Laws concerning Magnetic Fields

2.2.1 Inverse Cube Law

The inverse cube law states that the magnetic field of a dipole magnet decreases with the inverse cube of the distanc (Michaud [2013], Liang et al. [2012], Chan et al. [2013]).

2.2.2 Ampère's circuital law

Current produces a magnetic field.

According to Ampère's (circuital) law, when current runs through a conductor, it produces circular magnetic field around the conductor, that is directly proportional to the current (Matsushita [2014], Weik [2000]). Thereby, the current's flow direction predetermines the direction of the magnetic field lines, as shown in Figure 2.2. The stronger the current is, the denser the magnetic field lines and the stronger the magnetic field.

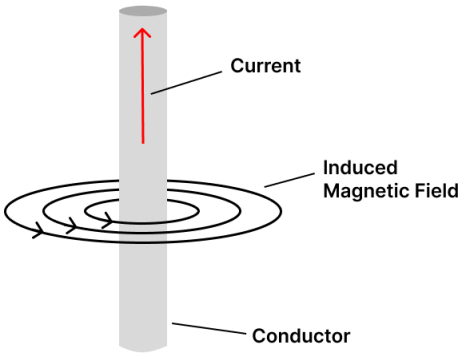

Figure 2.2: A visualization of Ampère's circuital law, where current and its direction is marked in red, while the induced magnetic field is indicated by cylindrical black lines.

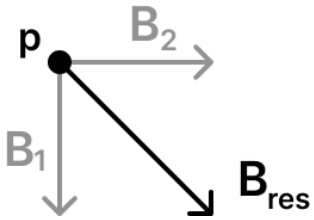

Figure 2.3: When two applied magnetic field vectors $\mathbf{B}_1$ and $\mathbf{B}_2$ at a point p superimpose, the resulting magnetic field at p is $\mathbf{B}_{res}$ = $\mathbf{B}_1$ + $\mathbf{B}_2$, according to the superposition principle.

2.2.3 Superposition Principle

Magnetic fields underlie the superposition principle (Gan [2022]), which according to Campos et al. [2021]) states that "the net response of a number of stimuli is the same as the sum of all individual responses" (p. 63). For an example in the context of magnet fields, see Figure 2.3.

2.3 Magnetic Field Space

Chen et al. [2013] defined a $magnetic\ field\ space$ to describe the magnetic field that is applied to a magnetic field sensor, the sensor being at the origin. The magnetic field strength at a location in space is determined by (r, θ), where r is the distance between the magnet and the sensor, and θ is the

We describe the 3D magnet location by the sensor-magnet distance and the magnet angle.

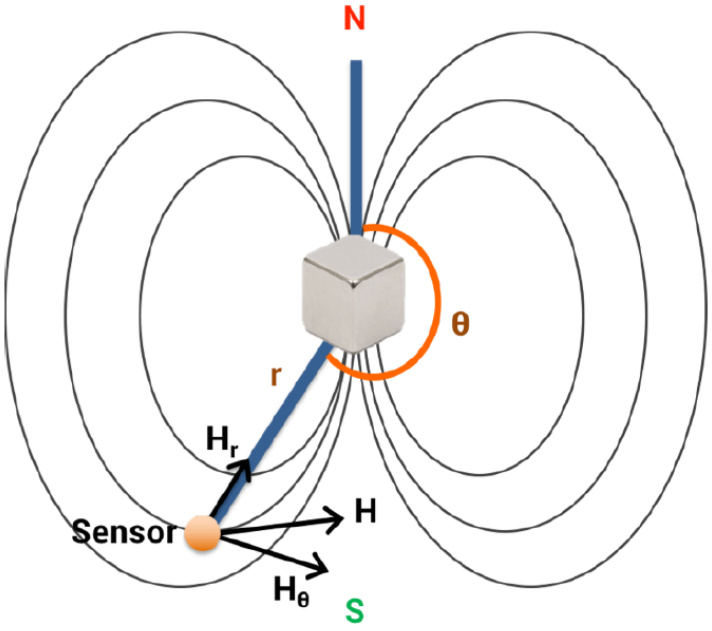

Figure 2.4: Chen et al. [2016] specified the 3D location of a magnet in space by the distance between the sensor and the magnet r and the angle between the sensor and the north pole θ. Figure by Chen et al. [2016].

angle between the magnet's north pole and the sensor (See Figure 2.4). According to the authors, a third dimension is not needed, because the magnetic field of the magnet is symmetric around the north pole. In this thesis, we will use (r, θ) to describe the magnet's position in space instead of the magnetic field strength.

Chapter 3

Related Work

Our approach lies in the intersection of different research domains, including magnetic tracking and gesture recognition. In the following, we briefly summarize previous research in each of these areas in order to give a proper overview.

3.1 Approaches Based on Magnetic Tracking

The idea of magnetic field detection has been used in the field of human-computer interaction before.

GaussStarter features a modular Hall Sensor grid that allows for prototyping and an adjustable sensing area.

Liang et al. [2015] introduced GaussStarter, a modular Hall sensor grid (Figure 3.1a) that is easily expandable using breadboards (Figure 3.1b). Each hardware module is 2cm x 2cm x 1cm in size and embeds sixteen Hall sensors. The thickness of the module can be brought down to 2mm. By tiling the sensor grid units on a breadboard, they made the sensing area easily adjustable for further approaches like Liang et al. [2012] and Liang et al. [2013]. Their provided software covers firmware that requests sensor data of each module and 2D position estimation using bi-cubic interpolation. While the idea of a sensor grid is fairly straightforward, the modular approach laid a good foundation for fu-

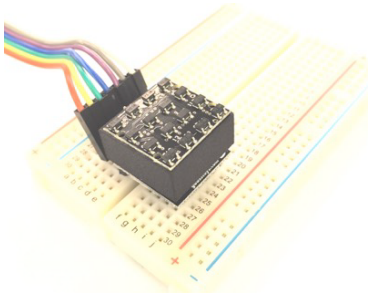

(a) A figure by Liang et al. [2015] showing their analog Hall sensor grid module that is connectable with a breadboard.

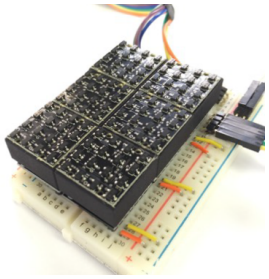

(b) Tiling the sensor grid modules on a bread board extends the sensing area (Figure by Liang et al. [2015]).

Figure 3.1: Figures showing GaussStarter by Liang et al. [2015].

GaussStarter does not involve sensor calibration.

ture approaches. However, we are constantly surrounded by an ambient magnetic field that biases the sensors, which makes sensor calibration necessary. However, GaussStarter does not include sensor calibration.

GaussSense enables digital drawing by combining GaussStarter with a magnetic pen. It involves sensor calibration via offset subtraction.

Building up on that, Liang et al. [2012] introduced GaussSense, a back-of-device sensing interaction technique for enabling input on arbitrary surfaces by using a magnetic stylus; to improve digital sketching experiences. Figure 3.2a illustrates a typical setup of GaussSense. In this work, Liang et al. [2012] used GaussStarter and combined it with a stylus that has a magnet embedded into it. In contrast to GaussStarter, they calibrated the sensors before operation. Their calibration is made up of precomputing an offset for each sensor by averaging a hundred magnetic field measurements. When a magnet hovers over the sensor grid in operation, they interpolate the measurements to reconstruct the shape of the magnetic field. Based on its estimated shape and the sensor measurements, their approach is able to track the 2D position of the stylus among other things like tilt, hover and pressure sensing. Figure 3.2b shows the way sensor activation areas vary depending on the tilt, hover and pressure of the stylus. For 2D position estimation, they used the bi-cubic interpolation algorithm provided by GaussStarter. Lastly, they applied this setup to the back of a screen, so that the stylus can be slid smoothly across it.

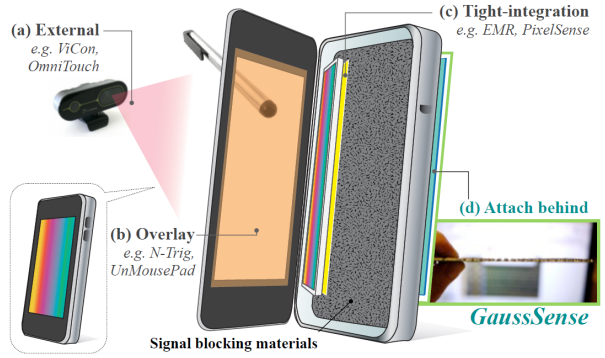

(a) This figure by Liang et al. [2012] shows an application of GaussSense. The Hall sensor grid can be attached to the back of a device, so that the magnetic stylus can be directly used on the screen of the device, extending its functionality.

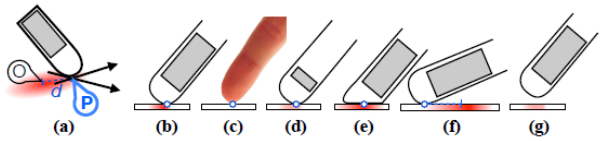

(b) The magnetic field intensity perceived by the sensors is illustrated by a red color. GaussSense is able to differentiate between a variety of events, including stylus events (b), touch events (c), a different stylus (d), various pressures (e), different tilt angles (f), and hover (g). Note that the shape of the magnetic field and its intensity differs with the hover, tilt and pressure of the stylus (Figure by Liang et al. [2012])

.

Figure 3.2: Figures by Liang et al. [2012].

FingerPad uses a Hall sensor grid for gesture recognition in mobile applications.

Chan et al. [2013] introduced FingerPad, a nail-mounted device that turns the tip of the index finger into a touchpad; allowing private and subtle gestural interaction in mobile applications. They placed a sensor grid on the index finger nail, while a magnet is located on the thumbnail (See Figure 3.3). Their approach recognizes gestures typical for smartphone user interfaces. It supports gesturing numbers as well. The sensor grid is 12mm x 12mm in size, where the sensors are separated by 2mm. They used a 3mm-diameter x 8mm-height cylindrical neodymium magnet that allows effective sensing in the range of 2.1cm from the sensor plate. Unlike GaussSense, FingerPad cannot perform cal-

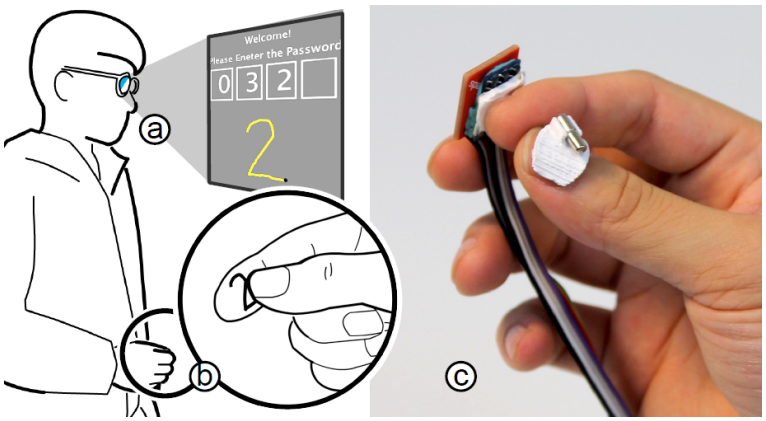

Figure 3.3: An application of FingerPad, where the magnet is located on the thumb nail while the Hall sensor grid attached to the index finger nail (c). This setup gestural input like numbers (b) that can only be seen by the user when wearing smart glasses (a). Figure by Chan et al. [2013].

Sensor calibration does not make sense for mobile applications.

ibration by subtracting an offset. This is because the pre-computed offset is specific to the position and orientation of each sensor, which both change all the time when people are moving their hands. Instead, Chan et al. [2013] matched finger pad coordinates to sensor grid coordinates. They calibrate their setup by taking nine measurement points on the finger pad. Based on this data, they extract a homographic transformation that maps finger pad coordinates to sensor-grid coordinates. A bi-linear position estimation algorithm is then applied in the sensor-grid coordinate space.

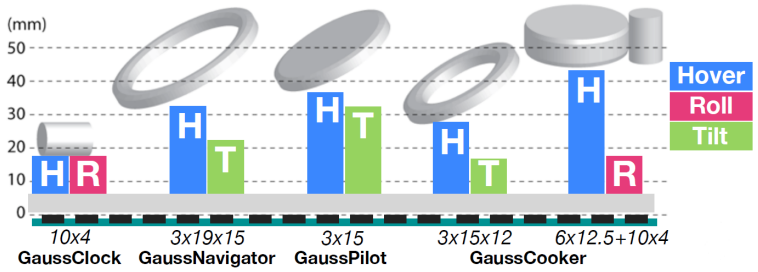

Figure 3.4: Different GaussBits with corresponding distances in which the hovering position and respectively the tilt and roll direction can be resolved. Figure by Liang et al. [2013].

Liang et al. [2013] achieved the largest input distance with 44mm in their papers about GaussBits, which is based on GaussStarter (Liang et al. [2015]). A GaussBit is an object

that embeds a magnet. They compared the reliable input distances of each GaussBit in respect to the maximal sensing distance when hovering, tilting and rolling it over the Hall sensor grid. (See Figure 3.4).

Meier et al. proposed using a Hall sensor array for smart home applications.

Meier et al. [2019] proposed the concept of a magnetic field sensor array as a universal smart home device; distinguishing different gestures and aiming to increase its acceptance by elderly people. They embedded a 5mm x 5mm x 5mm magnet into a 3D printed ring and trained a neural network to distinguish the angular position of the magnet around the sensor. Their classification results are shown in Figure 3.6.

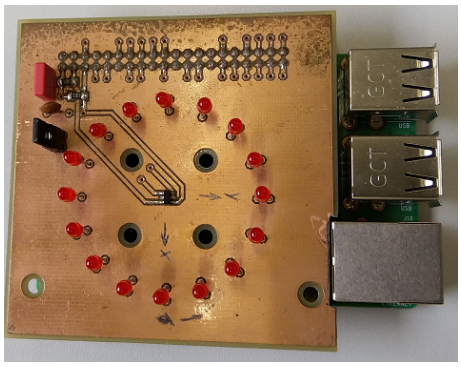

Figure 3.5: A Figure taken from Meier et al. [2019], showing their experimental prototype that embeds a single 3D Hall sensor.

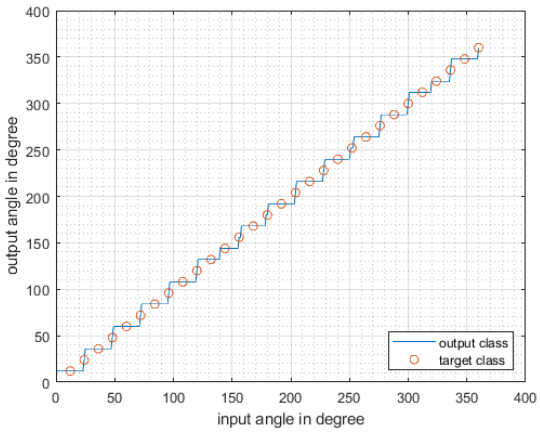

Figure 3.6: The classification results of the neural network trained by Meier et al. [2019].

Among other applications, they aimed to make dimming

light sources and adjusting the room temperature possible. They did not name the sensing range of their approach, but since Meier et al. [2019] used Hall sensors and Liang et al. [2013] reported a maximum sensing distance of 44mm with larger magnets, one can assume that it lies under 4cm in the prototype stage.

The maximal reported user input distance using Hall sensor grids is currently 14cm.

Across all papers using Hall sensors, we found the largest input distance in an article by Schlageter et al. [2001] with a distance of 14cm. The authors maximized the signal-to-noise ratio by minimizing the component-induced noise on their PCB and by amplifying the signals of the Hall sensors. They used a cylindric magnet with a diameter of 6mm and a height of 7mm. This magnet is larger than the magnets used by the previously mentioned approaches, so a higher sensing range is to be expected.

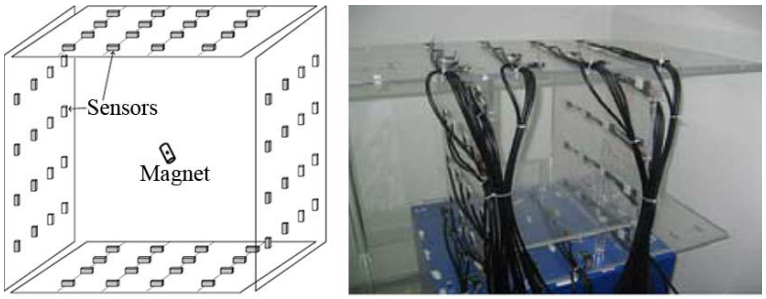

Figure 3.7: (a) A schematic illustration of the cubic magnetic sensor array. (b) shows the real sensor array. Figure by Hu et al. [2010].

Hu et al. use AMR sensors which yield a by far larger user input distance than Hall sensors.

A paper using a different type of magnetic field sensor was published by Hu et al. [2010]. They use Anisotropic magnetoresistance effect (AMR) sensors, which are more sensitive to magnetic fields than Hall sensors. Hu et al. [2010] introduced a cubic 3-axis magnetic sensor array; allowing real-time tracking of magnet position and orientation. They constructed a cube with sixteen AMR sensors on each side with a total size of 0.5m x 0.5m x 0.5m (See Figure 3.7). Their goal was to track objects inside the human body. Hence, their sensing range needed to be much larger compared to the previous approaches and lies between 5cm and 45cm for magnets as small as ∅4mm x 5mm. This distance is suitable for mid-air interaction and

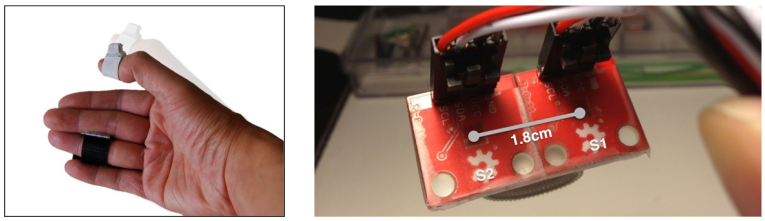

(a) (b)

Figure 3.8: (a) uTrack utilizes a magnet on the thumb in combination with a sensor grid containg two Hall sensors, enabling real-time 3D input. (b) The sensor grid containing two sensors with a fixed sensor distance, which is necessary to resolve ambiguity in their 3D position estimation algorithm. Figures by Chen et al. [2013].

therefore we chose to use AMR sensors as well.

uTrack uses only two sensors for accurate 3D position estimation, that is based on background knowledge about magnetic fields.

However, while some approaches conduct 2D position estimation by using plenty of sensors in combination with a simple position estimation algorithm, other approaches use only a fistful of sensors combined with a more complex algorithm. An approach that carried this to the extreme is uTrack by Chen et al. [2013]. uTrack is a 3D single-point tracking system; allowing subtle interaction in virtual environments and with computers. Similar to FingerPad, they position the magnet on the thumbnail, while the sensors are attached to the ring finger (See Figure 3.8a). They used only two sensors (See Figure 3.8b) to estimate the 3D position of the magnet in real-time with an average accuracy of 4.84mm. Also, they are able to track the tilt angle of the magnet in x, y and z direction. Their position estimation algorithm makes use of background knowledge about magnetic fields. Chen et al. reported the limits of their system as $\pm$ 80mm around the x-axis, $\pm$ 60mm around the y-axis and 0-80mm regarding the z-axis.

In contrast to Hall sensors, AMR sensors yield a sufficient user input distance for mid-air interaction.

While Chen et al. [2013] propose a promising approach, their sensing distance is far too small for mid-air interaction. The same holds for the approaches GaussStarter by Liang et al. [2015], GaussSense by Liang et al. [2012] and FingerPad by Chan et al. [2013] and the smart home control device by Meier et al. [2019]. While the setup by

Schlageter et al. [2001] could be barely used for mid-air interaction itself, the magnet is too big to be embedded into a ring. In contrast, our approach yields a user input distance of 15-20cm with a ∅8mm x 2mm disk magnet. While Hu et al. [2010] support a larger sensing range between 5cm and 45cm, their approach is not designed for gesture recognition and is too large to be embedded into the environment.

3.2 Gesture Recognition Approaches

Of course, there are gesture recognition approaches that do not involve magnets or magnetic field sensors.

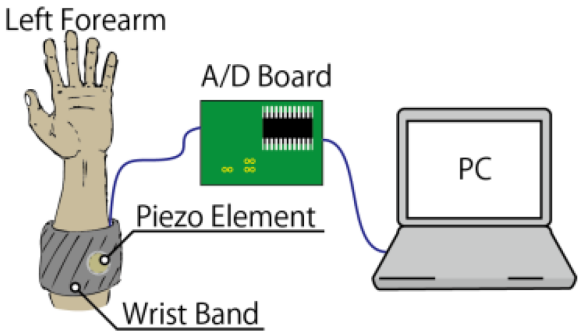

Figure 3.9: This figure by Yamakawa and Nojima [2012] illustrates their setup.

The wrist band by Yamakawa et al. perceives muscle acoustics in order to recognize gestures.

Yamakawa and Nojima [2012] proposed a novel hand-gesture recognition method based on mechanomyograms (MMG) using piezoelectric-based sensing; improving robustness from human motion and noise. As shown in Figure 3.9, they constructed a wrist band that embeds MMG sensors, which are able to perceive muscle vibration and muscle acoustics. Yamakawa and Nojima [2012] compared the performance of k-nearest neighbors, support vector machine, linear discriminant analysis and deep neural network algorithm on the task of gesture recognition. Among these, k-nearest neighbors yielded the highest gesture recognition accuracy. Their study was focused on eight different hand gestures designed for gaming purposes. They concluded that k-nearest neighbors yielded

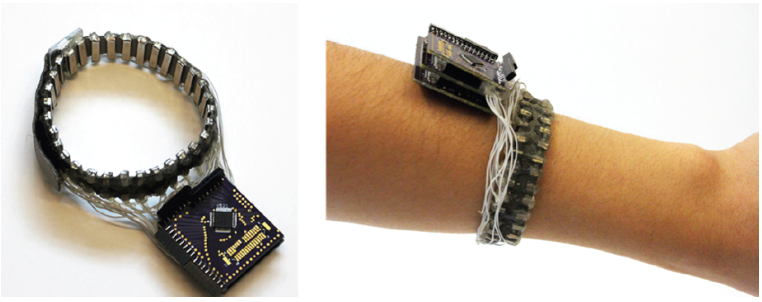

Figure 3.10: The electrode armband and the Electrical Impendance Tomography sensing board constructed by Zhang et al. [2016].

the highest accuracy with 94.56%.

The electrode wrist band by Zhang et al. recognizes pinching gestures by analyzing the interior wrist structure.

Zhang et al. [2016] introduced a system that uses Electrical Impedance Tomography offering non-invasive, high accuracy gesture recognition. Similar to Yamakawa and Nojima [2012], they constructed a wrist band embedding up to 32 electrodes (See Figure 3.10). Using Electrical Impedance Tomography, they are able to estimate the interior structure of an object, which is a wrist in their case. Based on machine learning and samples, their approach recognizes gestures from the embedded electrodes with 94.3% accuracy.

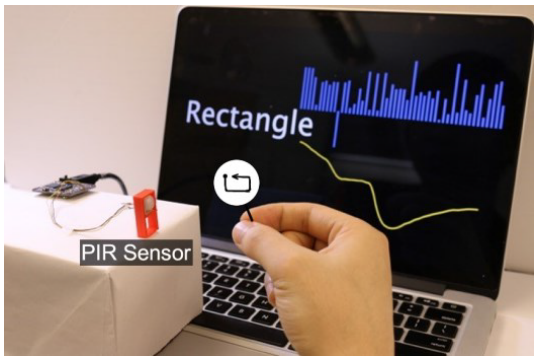

Figure 3.11: An example setup of Pyro. Using an passive infrared sensor (PIR), Pyro is able to conduct micro thumb-tip gesture recognition. Figure by Gong et al. [2017].

Pyro recognizes micro thumb-tip gestures with an infrared sensor.

Gong et al. [2017] presented Pyro, a micro thumb-tip gesture recognition technique based on thermal infrared signals radiating from the fingers; making it suitable for wearable and mobile applications. An example setup is shown in Figure 3.11. It is made out of an infrared sensor, a camera, hardware and software for gesture recognition. Like the previous approaches, they used machine learning for gesture classification of fine thumb-tip gestures. Gong et al. conducted studies to prove its robustness to ambient lighting changes and background hand movements. However, changing hand temperature significantly affected the gesture recognition accuracy. In a study, their approach recognized six gestures with a cross-validation accuracy of 93.9%. The optimal sensing distance of their system lies between 0.5cm and 30cm away from the infrared sensor.

In contrast to our approach, the discussed approaches are too restricted in the recognizable gestures and lack comfort of use.

In contrast to our approach, these approaches cannot be seamlessly integrated into the environment. All of the mentioned approaches require a power source (e.g., a battery), which leads to an increased weight of the device and additionally leads to heat generation. Pyro by Gong et al. [2017] has a sensing range that is suitable for mid-air interaction, but their recognizable gestures are limited to micro thumptip gestures. A drawback of the MMG-based wrist band by Yamakawa and Nojima [2012] is that the sensors need to be positioned at a specific position on the forearm, where it needs to be fixed tightly, so that the sensors do not move. This could be uncomfortable for users. The wrist band by Zhang et al. [2016] does not need to be positioned as accurately, but their identifiable gestures are limited to pinching gestures of each finger.

The $1 recognizer could be used for 2D gesture recognition on our setup.

Our setup, on the other hand, is able to support 2D gestures of all kinds, for example by applying the $1 gesture recognizer by Wobbrock et al. [2007]. This algorithm is simple, fast, and short with about 100 lines of code; enabling novice programmers to incorporate gestures into their prototypes. Figure 3.12 shows a subset of gestures that the $1 recognizer is able to distinguish. Our approach is designed around this algorithm, but it has not yet been applied in this work.

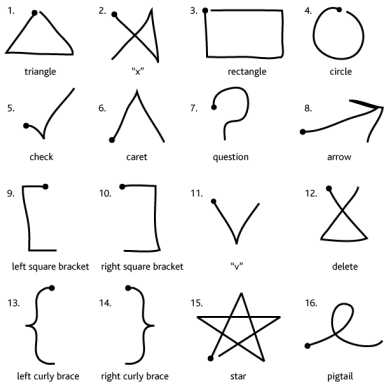

Figure 3.12: A subset of gestures recognizable by the $1 algorithm. Figure by Wobbrock et al. [2007].

3.3 Ring Interaction Insights

We propose a ring to be used as an input device for our approach in the future.

Everyday objects like rings, necklaces, or bracelets are commonly used in HCI research. This is not only because these objects bring comfortable usability, but also because people are familiar with those kinds of objects, which makes wearing such devices socially acceptable. Since people are able to perform precise gestures with their hands, we propose that a ring as an input method would suit our setup the best. Other benefits are that one's hand can still be normally used when wearing a ring and it's easy to put on or off. We will not tackle the construction of a magnet-embedded ring in this thesis, but since we plan to do so in the future, we will briefly look into user preferences.

Users prefer to wear a ring at the base of the index or middle finger.

Gu et al. [2019] tested different ring wearing positions and tapping postures with a ring using an Inertial Measurement Unit (IMU) sensor; improving the accuracy of contact sensing. Figure 3.13 shows the tested ring wearing positions and results. Gu et al. [2019] found that users preferred wearing the ring on the proximal phalanx of the index or middle finger. These results indicate that, in the future, the magnet-embedded ring of our setup should be worn at one of these positions as well.

For further information on ring-based gesture input, we refer to the systematic literature review by Vatavu and Bilius [2021].

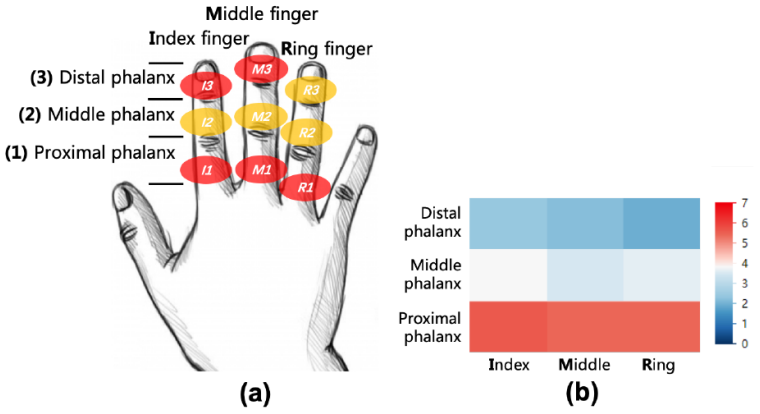

Figure 3.13: (a) illustrates different ring wearing positions on the index finger, middle finger and ring finger with a denotation for each position. (b) shows the user preference of each ring position (0 = worst, 7 = best). Figures by Gu et al. [2019].

Chapter 4

Setup Requirements

Before designing the magnetic field sensor grid, we need to specify the requirements of our system.

As stated previously, our setup should be suitable for gesture recognition by using the $1 recognizer by Wobbrock et al. [2007] or a similar approach. Since this algorithm is able to recognize 2D gestures based on a sequence of 2D positions, it is sufficient when our system can provide such a sequence.

The setup needs to support sufficiently accurate 2D position estimation.

The setup should support mid-air interaction and a height range, in which the user can perform gestures easily, in conjunction with a suitable sensing area. Since the optimal area depends on the applications, it should be expandable.

Mid-air interaction must be possible and the sensing area should be adjustable.

In the following, we are going to specify the requirements in more detail.

4.1 Sensing Range

A sensor cannot perceive a magnet at an arbitrary distance: When it is moved too close to the sensor, the sensor overdrives and when the magnet is too far away, the applied magnetic field at the sensor is too weak to be distinguish-

able from noise. Therefore, the operation range of the sensor is restricted by the overdrive distance d_{min} and the maximal sensing distance d_{max}.

Definition: *Sensing Range*

SENSING RANGE:
The range [d_{min}, d_{max}], where d_{min} corresponds to the overdrive distance and d_{max} corresponds to the maximal sensing distance (See Figure 4.1).

4.1.1 Overdrive Distance d_{min}

Overdriving the sensor can permanently damage it.

We say that a sensor overdrives when the sign of at least one axis measurement changes rapidly, when spikes occur regularly or when the reported magnetic field clips at a specific value. Depending on the sensor, overdriving it can permanently damage it or alter its functionality.

Definition: *Overdrive distance* d_{min}

OVERDRIVE DISTANCE d_{min}:
The distance between the sensor and the magnet below which the sensor overdrives.

Hence, a given magnet can not be moved arbitrarily close to the sensor. Stronger magnets yield a larger overdrive distance than weaker magnets.

4.1.2 Maximal Sensing Distance d_{max}

As explained in Section 2.3, the applied magnetic field at a sensor S is dependent on the magnet orientation θ and the distance d between the magnet and the sensor.

Definition: *Maximal Sensing Distance* d_{max}

MAXIMAL SENSING DISTANCE d_{max}:
The maximal distance under which the magnet can be perceived for all magnet orientations θ. For $d > d_{max}$, the applied magnetic field at S that is not distinguishable from noise.

4.2 Height range

The sensing range does not correspond to the height range, in which the position of the magnet can be reliably estimated.

HEIGHT RANGE:
The range $[h_{min}, h_{max}]$, in which the 2D magnet position can be estimated reliably, independent of d and θ (See Figure 4.1).

Definition: *Height range*

MINIMAL HEIGHT h_{min}:
The minimal height h_{min} corresponds to the minimal sensing range d_{min} (See Figure 4.1).

Definition: *Minimal height h_{min}*

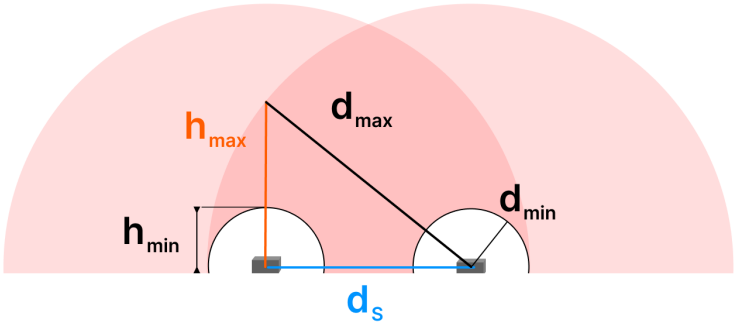

Figure 4.1: A comparison of the sensing range $[d_{min}, d_{max}]$ and the height range $[h_{min}, h_{max}]$, where the sensing range (pink area) is defined in respect to the sensor and the height range is defined in respect to the sensor grid. The maximal height h_{max} is dependent on d_{max} and the sensor spacing d_S.

4.2.1 Maximal Height h_{max}

The maximal height h_{max} differs significantly from d_{max} for most sensor spacings. As demonstrated by Chan et al. [2013], the position of a magnet M can only be estimated at a point p, where at least two sensors perceive M. When only one sensor perceives M, the position of M is ambiguous. Thus, we define h_{max} as the maximal height over a sensor, under which the 2D position of the magnet can be

Reasoning for the definition of h_{max}.

estimated (See Figure 4.1). Note that this definition yields an air cuboid, in which 2D position estimation is definitely possible. h_{max} is determined by:

Definition: *Maximal height* h_{max}

MAXIMAL HEIGHT h_{max}:

$$h_{max} = \sqrt{d_{max}^2 - d_S^2} \tag{4.1}$$

where d_S is the sensor spacing.

h_{max} can differ significantly from d_{max}.

With a small sensor spacing, h_{max} is close to d_{max}, but when the sensor spacing becomes large, they deviate significantly. See Figure 4.1 for a comparison of the sensing range and the height range.

4.2.2 Desired Height Range

Desired Minimal Height h_{min}

Overdrive must not occur in applications, so the overdrive distance may be maximally 2cm.

As mentioned previously, h_{min} is equal to the overdrive distance d_{min}. An example application, in which the sensors might be overdriven, is the application of the sensor grid on the underside of the tabletop. If the overdrive distance d_{min} is larger than the thickness of the tabletop, the sensors might be overdriven when the magnet-wearing hand is put on the desk close to a sensor. Desks are typically around 2cm thick, so the overdrive d_{min} needs to be equal or less than 2cm. When it is a bit greater than that, a spacer could be used to increase the distance between the sensors and the underside of the table.

Desired Maximal Height h_{max}

To choose a magnet that yields an appropriate maximal height h_{max}, we need to consider user behavior in the context of possible sensor grid applications.

Optimally, h_{max} is equal to or larger than 30cm.

For example, when sitting at a desk, the user's hand will

be located higher when propping their elbow. The average underarm length of men in Germany is around 30cm Rickert [2010]. Since men typically have larger bodies than women, we chose $h_{max} \geq$ 30cm. However, since people typically hold their propped underarm at an angle and not vertically, a lower h_{max} might be sufficient.

We will keep $h_{max} \geq$ 30cm in mind when choosing a magnet for experiments. If an application demands a lower h_{max}, for example in order to disregard unintended inputs, this can be configured by software. For a larger h_{max}, a stronger magnet, a more sensitive sensor, a lower sampling rate for longer sampling intervals or a larger amount of sensors for oversampling need to be chosen. Since overdriving the sensors might damage them, we will pay more attention to the overdrive distance h_{min} than to h_{max} when selecting a magnet.

When choosing a magnet, we pay more attention to h_{min} than to h_{max}.

4.3 List of Requirements

We summarized the system requirements in the following list:

(1) Expandable sensing area

(2) Overdrive distance (h_{min}) $\leq$ 2cm

(3) Feasible 2D position estimation of the magnet up to $h_{max} \geq$ 30cm

Chapter 5

Sensor Choice, Adapter PCB Design and Position Estimation

Now that we have defined the system requirements, we can pick out a magnetic field sensor that allows for mid-air interaction in the desired height range. To achieve that, we discuss sensor types and sensor characteristics, choose a sensor according to the these and talk about important properties of the chosen sensor.

We construct a modular sensor adapter PCB to allow for an adjustable sensing area and simple wiring, alignment and mounting. Then, we implement sensor communication and sensor calibration with an Arduino. Lastly, we examine the anisotropy of the sensor.

5.1 Choosing An Appropriate Sensor

Hall sensors and AMR sensors are magnetic field sensors.

There are a variety of ways to detect a magnetic field. One way is to use sensors based on magnetoresistance, which is the property of a material to change its electrical resistance when a magnetic field is applied Pippard [1989]. Examples of magneto-resistive sensors include Hall sensors and

anisotropic magnetoresistance (AMR) sensors.

AMR sensors are more sensitive than Hall sensors.

AMR sensors are more sensitive to magnetic fields than Hall sensors Tumanski [2013], Popovic et al. [2002], Ripka and Janosek [2010]. This means that AMR sensors are able to detect magnets from larger distances than Hall sensors. On the other hand, when given a magnet, this means that the overdrive distance of AMR sensors is larger than the one of Hall sensors due to improved signal-to-noise ratios.

We use AMR sensors, because they yield a larger sensing distance.

The largest sensing distance using Hall sensors that prior research achieved with a lot of effort was 14cm[Schlageter et al., 2001]. In contrast, AMR sensors were used in prior research to track magnetic material from distances as large as 50cm [Hu et al., 2010]. Since with determined the desired maximal height as $h_{max} \geq 30$cm, we chose to use AMR sensors for our setup.

We are going to discuss varying properties of AMR sensors and point out which characteristics are favorable for our setup. After that, we will give an overview about the AMR sensor of our choice.

5.1.1 Sensor Characteristics

1D Sensors vs. 3D Sensors

We use 3D sensors, because they yield more information than 1D sensors.

In this section, background knowledge from Section 2.1 about the **B**-field is required. When a magnetic field vector $\mathbf{B} = (\mathbf{B}_x, \mathbf{B}_y, \mathbf{B}_z)^{\mathrm{T}}$ is applied to a sensor, then 1D (or single-axis) sensors can only sense the vector component $\mathbf{B}_z$ while 3D (or 3-axis) sensors are able to measure all **B** components independently from each other.

Apart from their cost and power consumption, there is no disadvantage of 3D sensors compared to 1D sensors. Thus, we chose to use 3D sensors for our setup to have as much information about **B** as possible.

Analog vs. Digital

Sensors with digital transmission type are more suitable for our setup.

In regards of the transmission type, some sensors output the magnetic field as an analog signal, while others transmit it digitally. Although the efficiency of an analog signal is higher, it is also more prone to errors due to noise. Because the magnetic field decreases inverse-cubically with the distance (See Section 2.2.1), we are mostly working with measurements close to zero. At the same time, the sensor is surrounded by ambient noise and when mounting it on a PCB, every component on the signal path adds noise to the signal. When using analog sensors, this would worsen the signal-to-noise ratio. This problem is less prominent for digital sensors, which keep the analog components in the sensor to a minimum. Thus, we will be using a sensor with digital transmission type.

Other Considerations

Since we are working with measurements close to zero (See Section 2.2.1), we searched for sensors with a high resolution and with low self-induced noise. Also, we considered the sensor's linearity in the selection process, since distorted magnetic field values could affect the 2D position estimation performance. Furthermore, thermal influences can alter the sensor's reproduction of the magnetic field, so we focused on sensors with a built-in thermal induced offset correction.

5.1.2 The Chosen AMR Sensor

The 3-axis AMR sensor MMC5603NJ by Memsic meets the aforementioned criteria. It is 0.8mm $\times$ 0.8mm $\times$ 0.4mm in size, fairly cheap and supports 16bit, 18bit and 20bit operation modes with a resolution of 0.0625mG (10nT) per least significant bit. At 20bit operation mode, the sensor has a full scale range of $\pm$ 30G (3mT) (See Section 2.1 for the units).

The sensor is fairly linear, has low self-induced noise and eliminates the induced thermal variation offset.

The root mean square (RMS) noise of the sensor is 2mG (0.2µT) and spans the four least significant bits completely. Memsic reports a typical linearity error of 0.5% with a maximum of 0.75%. In addition, the sensor has a built-in and automatic SET/RESET function that eliminates the induced thermal variation offset and clears residual magnetization caused by strong external magnetic fields. The sensor may not be exposed to external magnetic fields stronger than 10.000G (1T) for a longer period of time, because doing so may permanently damage the sensor or may affect the sensor's reliability.

The sensor supports I^2C and I3C. Implementing I3C would be more beneficial.

Further, the sensor supports I^2C and I3C communication. It has four pins, including one for supply voltage (VCC), one for ground (VSA), one for the serial clock line (SCL) and one for the serial data line (SDA). While I^2C is currently more prevalent than I3C, I3C could facilitate coding and wiring on prototypes and on PCBs involving the sensors. This is because the sensor comes with a predefined static address which is the same for all sensors. When using I^2C, the sensor can only be addressed by its static address, making a multiplexer indispensable for both SDA and SCL. This leads to more cost and a higher effort for wiring and coding. On the other hand, I3C allows dynamic address assignment, which means that we can assign an individual address to each sensor. By that, multiplexers become superfluous, such that 128 sensors can be directly connected to a single controller and interconnecting the sensors is possible, which enhances the modularity of the sensor. It facilitates coding as well, since multiplexers do not need to be operated anymore.

See Appendix C for more information on the sensor.

5.2 The Sensor Adapter PCB

A modular sensor adapter PCB allows for an adjustable sensor spacing and sensing area.

Since the chosen AMR sensor is only 0.8mm × 0.8mm × 0.4mm in size, we needed to construct a PCB in order to conduct experiments with it. We could have constructed one PCB that embeds the whole sensor grid, but then we would have needed to predefine a certain sensor spacing.

Since we did not know if there was an optimal sensor distance or if the sensor distance influences the 2D magnet tracking results significantly, we chose to construct a modular sensor adapter PCB instead, which embeds one sensor each. This way, the sensor distance can be changed freely and similar to Liang et al. [2015] an adjustable sensing area is possible.

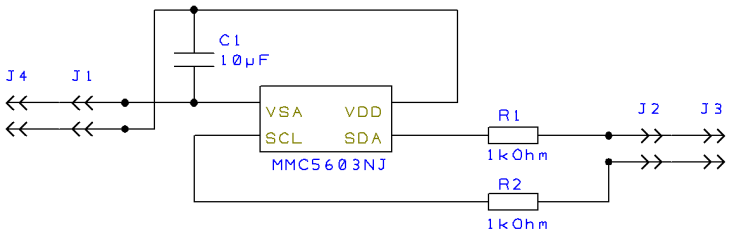

Figure 5.1: The schematic of the modular sensor adapter PCB for the 3-axis AMR sensor MMC5603NJ by Memsic, including the sensor itself, its periphery and connectors.

We chose the resistor values of the periphery in respect to our experimental setups.

Figure 5.1 shows the schematic of the sensor adapter PCB. It includes the AMR sensor, connectors and the sensor's periphery, which consists of a capacitor and two resistors. The capacitor secures a stable supply voltage, while the resistors protect the sensor from current surges. Since the data sheet recommended 2.7kOhm resistors for an I^2C bus with an length of less than 10cm and our experiments require wiring longer than 10cm, we chose 1kOhm resistors.

The PCB includes several features for prototyping and experiments.

Figure 5.2 and Figure 5.3 show the assembled and unassembled sensor adapter PCB. To facilitate experimental setups, we made sure to include mounting possibilities like two screw holes and four holes on the PCB edges for pin strips. By that, the PCB can be physically mounted on wooden boards or a breadboard. We chose angled connectors with reverse polarity protection, in order to decrease the risk of damage or malfunction, to avoid obscuring the area over the PCB and to facilitate mounting procedures with the sensor pointing upwards. Note that the holes currently used by connectors can also be used for pin headers with 2.54mm spacing, making breadboard mounting possible. Similar to Liang et al. [2015], this lays the groundwork for an adjustable sensing area.

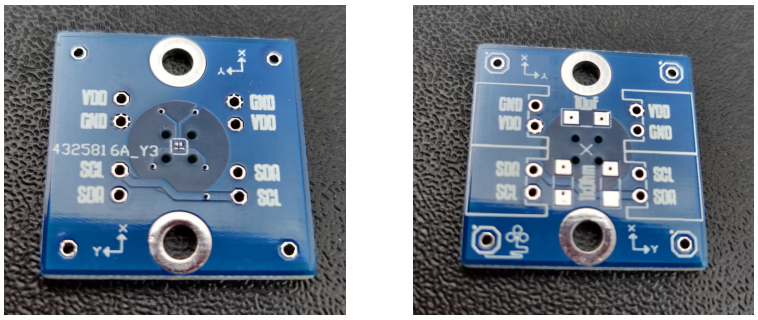

Figure 5.2: The **unassembled** sensor adapter PCB (left: top, right: bottom).

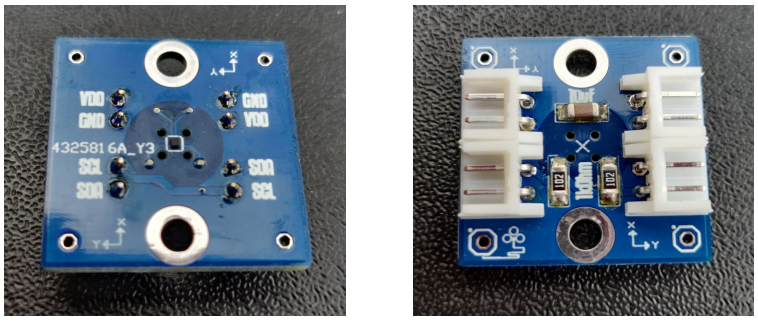

Figure 5.3: The **assembled** sensor adapter PCB (left: top, right: bottom). Note that the AMR sensor is located in the center of the top-side and the periphery is located on the bottom-side.

The silkscreen conveys useful information.

We designed the silkscreen to indicate the resistor and capacitor values, pin A1 of the sensor, the x-axis and y-axis as stated in the sensor data sheet, the location of the sensor on the bottom side of the PCB and the nets (VDD, GND, SCL, SDA). While the ground pin was declared as VSA in the data sheet, we decided to call it GND on the PCB, since this abbreviation is more commonly used for ground and is more intuitive as well.

We dealt with induced magnetic fields close to the sensor.

Ferromagnetic metals influence magnetic field lines (Matsushita [2014], Hook et al. [2009], Liang et al. [2012]). Because capacitors and resistors contain ferromagnetic materials, we placed the sensor and the other components on opposite sides.
According to Ampère's circuital law, when current runs through a trace, a magnet field is induced (See Section 2.2.2). Because of the high sensitivity of the sensor, we took care to optimize the traces in order to keep the inductive

interference as low as possible. The highest current runs through the nets VDD and GND for the current supply of the sensor. Because these traces connect directly to the sensor, we routed the supplying traces as close to each other as possible (See Figure 5.2). Since their current flow direction is opposed and the superposition principle holds for magnetic fields (See Section 2.2.3), the respective magnetic field of the traces cancel each other out to some degree in the region of the sensor (See Figure 5.4).

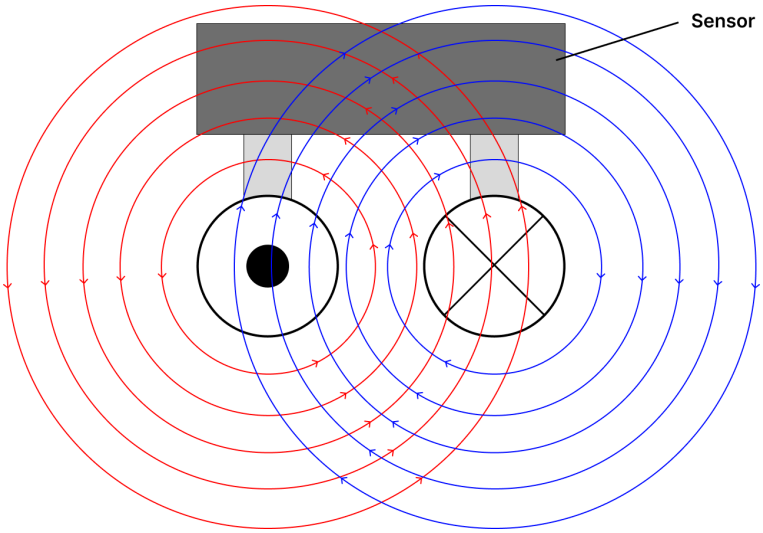

Figure 5.4: The induced magnetic fields of the wires supplying the sensor (left with inner circle = incoming current, right with cross = outgoing current). Note that, the magnetic fields start cancelling each other out to some degree in the region of the sensor, which results in a weakened magnetic field.

The influence of noise and further magnetic fields on the sensor is kept minimal.

Moreover, we created a ground plane and a voltage supply plane for various reasons. Firstly, the two planes form a giant capacitor, which lowers the influence of (external) noise on the circuit (Wang et al. [2006], Meng and Saleh [2009]). Secondly, each PCB trace has a resistance, which is related to the amount of thermal noise that the resistor creates when current passes through it Teel [2005]. A smaller resistance yields less thermal noise, so a copper plane is favorable in that aspect.
Note that both copper planes have a circle punched out with the sensor as the center of the circle. This serves two purposes: For one it is as a further protection from PCB in-

duced magnetic fields and secondly, it makes sure that as least noise as possible is transferred from the copper planes to the sensor by cross-talk.

5.3 Controlling the Sensor

We used an Arduino to operate the sensor, but it is not directly connectable to the sensor.

We used an Arduino Uno as a controller. It is capable of I^2C communication, but does not support I3C. It operates the sensor through its pins SCL and SDA. However, directly connecting the Arduino and the sensor is not possible, because of incompatible operation voltages. The upper limit of the sensor operation voltage is 3.6V, which is also the upper limit for the I/O pins of the sensor. On the other hand, the I/O pins of the Arduino are set to a voltage of 5V when sending a digital 1. If the Arduino is directly connected to the sensor, the sensor will be damaged and no longer operable.

We use level shifters to connect the Arduino with the sensor.

For this reason, the signals between the sensor need to be translated from 5V to 3.3V and vice versa. The circuit that fulfills this task is called level shifter. While a bi-directional level shifter is needed for SDA, a uni-directional level shifter is sufficient for SCL. With this setup, the Arduino operates the sensor and instructs it to take a magnetic field measurement. The corresponding Arduino code can be found in Appendix C.

5.4 Sensor Calibration

We need to calibrate the sensors, because of the ambient magnetic field.

We are constantly surrounded by an ambient magnet field induced by the earth (Haverinen and Kemppainen [2009]), which is strong enough for the sensor to pick up on. Since we only want to measure the magnetic field of the magnet, we need to subtract the ambient magnetic field in order to center the measurements of the sensor around zero:

$$\mathbf{B}_{calibrated} = \mathbf{B}_{measured} - \mathbf{B}_{ambient} \tag{5.1}$$

However, we do not know the ambient magnetic field, so we need to derive it from magnetic field measurements of the sensor. A straightforward method to determine $\mathbf{B}_{ambient}$ is to take one magnetic field measurement $\mathbf{B}_{measured}$ and assign $\mathbf{B}_{ambient} = \mathbf{B}_{measured}$. We tested this method in practice, but every measurement has a noise component, so $\mathbf{B}_{calibrated}$ was not zero. A second approach is to determine $\mathbf{B}_{ambient}$ by averaging a hundred measurements, similar to Liang et al. [2012]. When testing this approach, the deviation from zero was not as large as the one from the first approach, but it was still noticeable.

Noise hinders us to determine the ambient magnetic field appropriately by taking one measurement or averaging a hundred.

As a third approach, we determine $\mathbf{B}_{ambient}$ over time, based on a learning rate $\tau \in (0, 1)$ and a threshold $B_{threshold} \in \mathbb{N}$. We define $\mathbf{B}_{measured,t}$ as the sensor measurement of S at time t. Then, we determine $\mathbf{B}_{ambient}$ by:

We determine the ambient magnetic field by a machine learning approach.

$$\mathbf{B}_{ambient,t+1} = \tau \cdot \mathbf{B}_{ambient,t} + (1 - \tau) \cdot \mathbf{B}_{measured,t} \quad (5.2)$$

Note that both the previous value of $\mathbf{B}_{ambient}$ and the new measurement are used to compute the new value of $\mathbf{B}_{ambient}$. Equation 5.2 is repeatedly evaluated until every component of $\mathbf{B}_{calibrated}$ is smaller than $B_{threshold}$ held for a hundred time steps. After calibration, $\mathbf{B}_{calibrated}$ is centered around zero (See Figure 5.5). During experimenting, we found that the noise at each component was in the bounds of $\pm$ 8[mG]. Therefore, we chose $B_{threshold} = 10$ and further $\tau = 0.9$, because it seemed to yield satisfactory results.

5.5 Examining the Sensor's Anisotropy

The anisotropy of the sensor could impair the performance of applied 2D position estimation algorithms. For that reason, we examined it with the setup shown in Figure 5.6.

We took two semicircle measurements around the sensor: One that is aligned to the x-z plane and one that is aligned to the y-z plane (See Figure 5.6a).

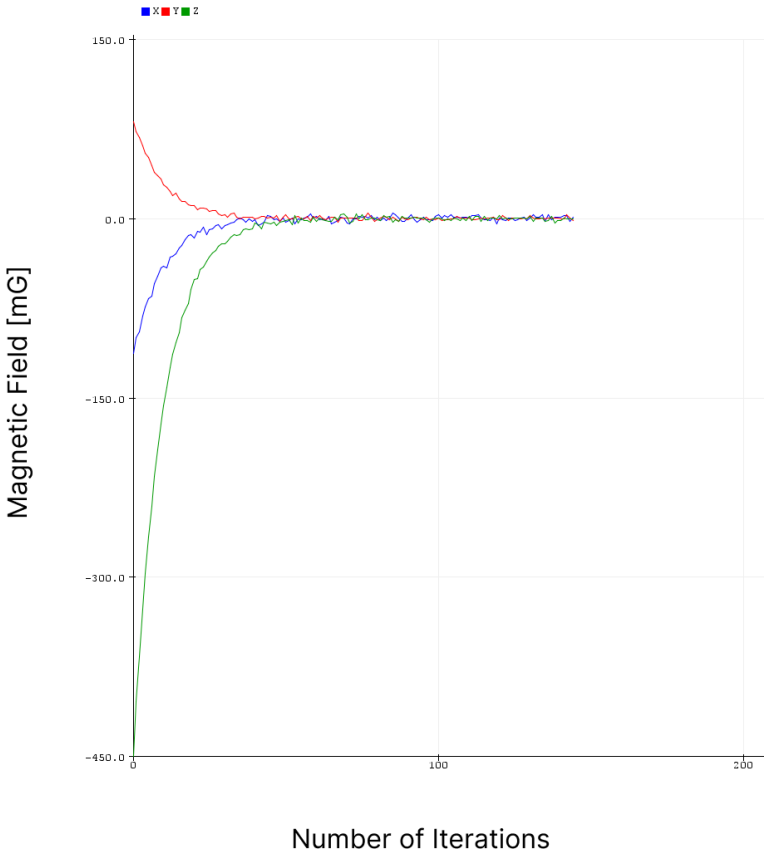

Figure 5.5: An example calibration of the 3-axis AMR sensor MMC5603NJ by Memsic.

For the following notation on r and θ, see Section 2.3. The sensor PCB is attached perpendicular to the edge of a plank (See Figure 5.6b). We declare the angle between the plank's edge and the magnet as α and take magnetic field measurements from $\alpha = 0°$ to $\alpha = 180°$ with a 10° step size between measurements, $r = 5$cm and $\theta = 0°$ for each measuring operation. To emphasize differences and reduce the influence of noise, we used a fairly strong magnet with a size of 5mm $\times$ 5mm $\times$ 5mm with an overdrive distance smaller than 5cm (See Table 6.1). For measuring the semicircle aligned to the y-z plane, we turned the sensor 90 degrees around the z-axis and repeated the procedure.

Figure 5.6c shows the results of the semicircle measurements. For both axis, the sensor features a local sensitivity peak at 90 degrees and grows more sensitive when moved

to the extremes of $\alpha = 0°$ and $\alpha = 180°$. However, when the experiment is repeated with a weaker applied magnetic field, the results are more balanced. This indicates non-linearity between the applied **B**-field and the sensor measurements.

There is a non-linearity between the applied magnetic field and the sensor measurements.

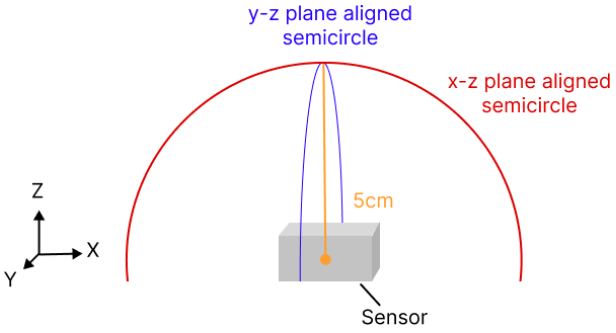

(a) The semicircles that are respectively aligned to the x-z plane and y-z plane. Measurements are taken along each semicircle to examine the anisotropy of the sensor.

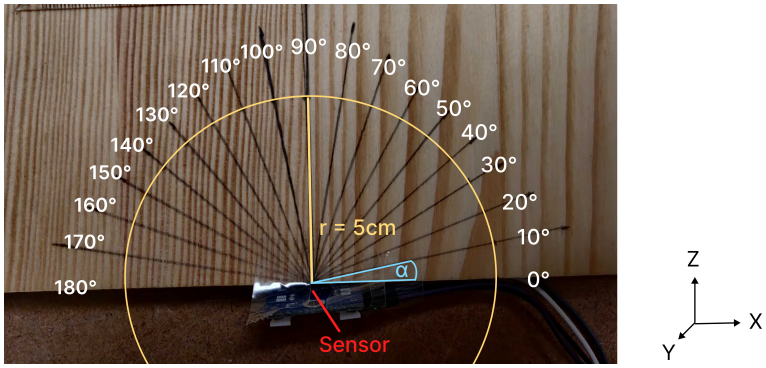

(b) The setup for the x-z plane aligned semicircle measurement. The semicircle has a radius of r = 5cm and a measurement is made every 10 degrees with $\theta = 90°$. The y-z plane aligned semicircle measurement is similarly done by turning the sensor 90 degrees along the z-axis.

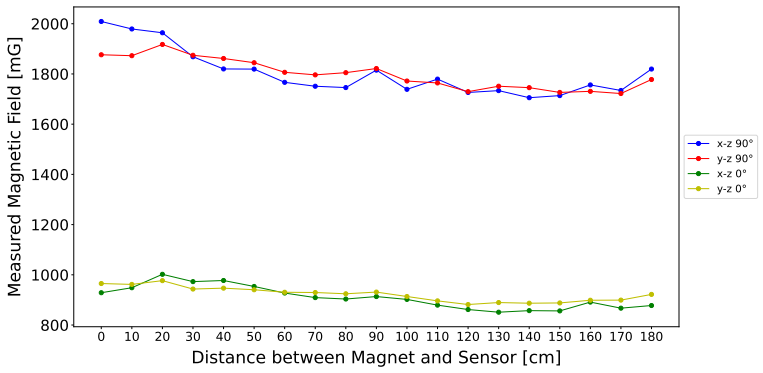

(c) The measurements along the semicircles that are aligned to the x-z plane and y-z plane. Each semicircle is measured two times: Once, such that the magnetic field of the magnet at the sensor is maximized ($\theta = 90°$) and once, such that it is minimized ($\theta = 0°$).

Figure 5.6: The setup and the results of the semicircle measurements.

Chapter 6

Magnet Selection

In the last chapter, we chose a sensor and made magnetic field measurements possible. Furthermore, in Chapter 4, we determined the desired height range as [$h_{min} \leq$ 2cm, $h_{max} \geq$ 30cm], where the overdrive distance h_{min} needs to be payed more attention than the maximal height h_{max}.

In order to find a magnet that results in the desired height range, we need to examine multiple magnets. In this chapter, we select magnets with a range of maximal sensing distances d_{max}, we examine their overdrive distance and their magnetic field progression up to 30cm from the sensor, we discuss the results and based on these, we choose a magnet for our setup. Additionally, we determine h_{max} for the chosen magnet and draw consequences for the maximal sensor spacing.

6.1 Magnet Selection Considerations

To find a suitable magnet, we examine magnets with a range of maximal sensing distances d_{max}.

We only consider permanent magnets, which stay magnetized and have a persistent magnetic field. The strength of a magnet is influenced by its material, its volume and its remanence, where remanence is the residual magnetization of the material after the application of a magnetic field (Lovatt and Watterson [1999], Jackson [1991], Coey

[2002]). Currently, neodymium magnets are widely used because they are the strongest magnets that can be bought on the market (as stated by Rivadulla et al. [2014]). This means that when selecting a neodymium magnet and another magnet type of the same strength, the neodymium magnet will have a smaller volume. Since a smaller size is favorable for embedding the magnet into an everyday object like a ring, we exclusively examined neodymium magnets.

The magnetic field of all magnets is symmetric along the z-axis.

To cover magnets with different sensing distances, we kept the variance of the remanence as low as possible and only varied the volume. Furthermore, to ensure that the sensor spacing can be the same in the x and y direction, it is necessary that the shape of the magnetic field is symmetric around the z-axis. Therefore, we chose magnets with a quadratic or circular base and exclude rectangular bases (See Table 6.1).

6.2 Magnetic Field Progression Measurements

The overdrive distance was determined for each magnet.

We determined the overdrive distance for each magnet with a sensor (See Table 6.1 for the results). After this, the functionality of the sensor might be impaired, so we use a different sensor for the magnetic field examination.

For each magnet, we examine the magnetic field strength progression.

To avoid overdriving the second sensor, we start at the next distance increment that is bigger or equal to the overdrive distance. From there, we move the magnet centimeter by centimeter up to 30cm from the sensor. At each distance, we average a hundred magnetic field measurements $\mathbf{B}_j \in \mathbb{R}^3,\ j \in \{0,..,99\}$ to $\bar{\mathbf{B}} \in \mathbb{R}^3$ in order to minimize the influence of noise. Then, we map $\bar{\mathbf{B}}$ to its length $\|\bar{\mathbf{B}}\|$, which corresponds to the magnetic field strength at the sensor. The setup is shown in Figure 6.1.

For the following notation on r and θ, see Section 2.3. We chose the orientation θ for each magnet during the measurements, such that the magnetic field is symmetric

L(mm) x W(mm) x H(mm)	Volume(mm^3)	Remanence(T)	Overdrive Distance(cm)
2 x 2 x 2	8	1.44 - 1.47	0.5
4 x 4 x 4	64	1.44 - 1.47	1.3
5 x 5 x 5	125	1.44 - 1.47	1.7
6 x 6 x 6	216	1.41 - 1.43	2.0
7 x 7 x 7	343	1.41 - 1.43	2.2
3 x 3 x 1	9	1.44 - 1.47	1.0
4 x 4 x 1	16	1.44 - 1.47	1.5
4 x 4 x 2	32	1.44 - 1.47	2.0
5 x 5 x 1	25	1.44 - 1.47	1.5
5 x 5 x 2	50	1.41 - 1.43	2.3
5 x 5 x 3	75	1.33 - 1.36	2.5
8 x 8 x 2	128	1.44 - 1.47	3.2
Diameter(mm) x Height(mm)	**Volume(mm^3)**	**Remanence(T)**	**Overdrive Distance(cm)**
∅1.5 x 1	1.77	1.44 - 1.47	0.8
∅1 x 2	1.57	1.44 - 1.47	0.7
∅2 x 2	6.28	1.44 - 1.47	1.1
∅3 x 2	14.14	1.44 - 1.47	1.5
∅6 x 2	56.55	1.41 - 1.43	1.5
∅7 x 2	76.97	1.33 - 1.36	1.7
∅8 x 2	100.53	1.17 - 1.20	2.0
∅9 x 2	127.23	1.33 - 1.36	2.3
∅10 x 2	157.08	1.29 - 1.31	2.6

Table 6.1: The dimensions, volume, remanence and overdrive distance of all examined neodymium magnets. The upper part of the table summarizes the data for cuboid magnets, and the lower part for disk magnets.

around the z-axis. Therefore, the orientation was always θ = 90° for all magnets, with the circular or quadratic magnet base facing the sensor.

For a better overview of the results, Figure A.2 shows the magnetic field progression for disk magnets and respectively, Figure A.1 shows it for cuboid magnets. The results of all magnets are summarized in Figure 5.6c.

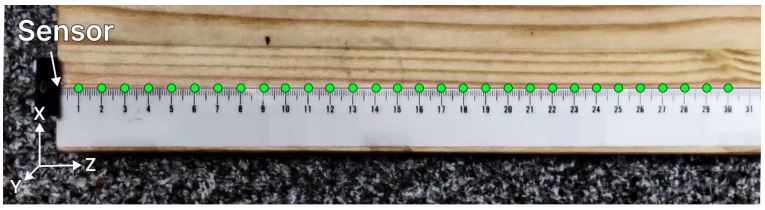

Figure 6.1: The setup for measuring the magnetic field of each sensor centimeter by centimeter up to 30cm from the sensor. The green points indicate measurement locations.

6.3 Discussion of Results

Sometimes, the sensor does not reproduce the magnetic field appropriately.

For most magnets, the measurement curve features a local low point close to the sensor. We have not found a definitive explanation for this, but we suspect that it could result from an overflow in the sensor register that contains the magnetic field measurement. This may lead to problems in 2D position estimation.

We picked the ∅8mm x 2mm disk magnet.

As a result, we chose the ∅8mm x 2mm disk magnet with an overdrive distance h_{min} = 2cm (See Table 6.1), and a sensing distance $d \geq$ 30cm for $\theta = 90$ (See Fig. A.2). Remember that h_{max} can be significantly smaller than d_{max}.

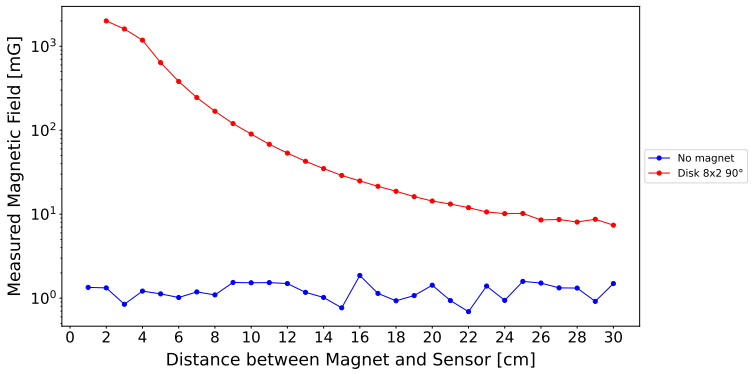

Figure 6.2: The magnetic field measurements of the **∅8mm x 2mm disk magnet** taken centimeter by centimeter starting from its overdrive distance up to 30cm from the sensor with an angle of θ = 0°. The figure has a logarithmic y-axis, such that values close to zero can be differentiated. For more information on the magnet, see Table 6.1.

6.4 Determining d_{max} and h_{max} for the Chosen Magnet

We determine d_{min} for the chosen magnet.

Prior research (Chen et al. [2013]) indicates that the weakest magnetic field is applied to a sensor at $\theta = 0$. To determine d_{max}, we examine the magnetic field progression of the chosen disk magnet at $\theta = 0$, with the same procedure as in Section 6.2. The result is shown in Figure 6.2.

Noise significantly influences the magnetic field measurements at $d \geq$ 25cm.

The result confirms that, the magnetic field is weaker for $\theta = 0°$ than $\theta = 90°$ for all corresponding measurement locations. The results suggest that the magnetic field of the turned magnet is significantly influenced by noise at around 25cm from the sensor. Thus, the signal-to-noise ratio is already too small at 25cm for sufficient performance of an applied 2D position estimation algorithm. Therefore, we assume $d_{max} \approx$ 25cm. For varying sensor spacings, we determined h_{max} by Equation 4.1 as illustrated in Figure 6.3.

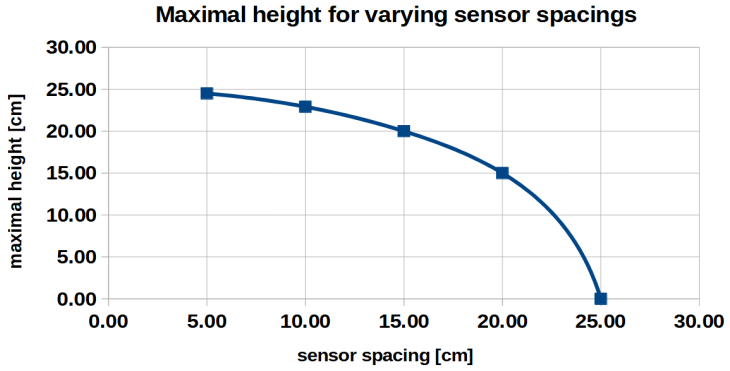

Figure 6.3: The maximal height h_{max} determined by Equation 4.1 with d_{max} = 25cm and sensor spacings $d_S \in \{5, 10, 15, 20\}$.

6.4.1 Implications for the Maximal Sensor Spacing

The maximal sensor spacing corresponds to h_{max}.

In the use case of applying the sensor grid on the underside of a tabletop while the magnet-wearing hand rests on its topside, the angle θ approaches 0°. When the sensor spacing is bigger than h_{max} and the magnet hovers over one

sensor, other sensors might not be able to perceive the magnet anymore. This might impair the results of applied 2D position estimation algorithms. Hence, the maximal sensor spacing d_S should be $\leq h_{max}$.

h_{max} lies between 15cm and 25cm for $d_S \in \{5, 10, 15, 20\}$ and we suggest a maximal sensor spacing of 20cm.

We tested several sensor spacings in Figure 6.3 and determined h_{max} = 15cm for d_S = 20cm. Since this is suitable for mid-air interaction and h_{max} decreases significantly for $20cm < d_S \leq 25cm$, we suggest 20cm as the maximal sensor spacing for the ∅8mm x 2mm disk magnet.

Chapter 7

Evaluation

We evaluate the system by 2D position estimation instead of 2D gesture recognition.

In this chapter, we examine if a sensor grid made out of the MMC5603NJ AMR sensor combined with the ∅8x2 disk magnet are suitable for applying gesture recognition algorithms like the $1 recognizer by Wobbrock et al. [2007]. Because such algorithms work with a sequence of estimated positions, we can examine the performance of an applied 2D position estimation algorithm, instead of examining the gesture recognition performance on our system. It is irrelevant whether the estimated positions are close to the real magnet positions, as long as the estimated positions appropriately reflect the input gesture.

7.1 Measurement Procedure

The position estimation algorithms are applied at 25 positions that cover a 2x2 sensor grid for varying sensor spacings and heights.

The accuracy of the estimated positions might be dependent on the sensor spacing and magnet height over the sensor grid. In the last chapter, we determined a maximal sensor spacing of 20cm, based on the ∅8x2 disk magnet. Hence, we evaluate applied 2D position estimation algorithms with sensor spacings d_S of 5cm, 10cm, 15cm and 20cm. For $d_S \leq$ 20cm, we determined h_{max} to be between 15cm and 25cm, so we evaluate heights of 5cm, 10cm, 15cm and 20cm for each sensor spacing. Further, we use a 2x2 sensor grid for our measurements, since results on a min-

imal sensor grid should be generalizable to larger sensor grids. For each sensor spacing and for each height, we estimate 25 magnet positions on a 5x5 grid that fully covers the 2x2 sensor grid (See Figure 7.2). The 5x5 grid is well suited, because it is the minimum size that contains all types of challenging positions: Corners, edges, the midpoint, positions with an equal distance to sensors on the x-axis, but not on the y-axis and vice versa.

The algorithms are applied on relative sensor and measurement positions.

For different sensor spacings, the measurement positions and the estimated positions are the same relative to the sensors, but the absolute positions are not (See Figure 7.1). In order to make the estimated positions for different sensor spacings comparable, we apply the position estimation algorithms to the relative positions:

Definition: *Sensor Positions (Relative)*

SENSOR POSITIONS (RELATIVE):
The position estimation algorithms are applied under the assumption of the sensor positions $S \in (\{0,1\} \times \{0,1\})^{2\times 2}$ with $s_{i,j} = (j,i)$ (See Figure 7.2).

Definition: *Measurement Positions (Relative)*

MEASUREMENT POSITIONS (RELATIVE):
For equidistant measurement positions and for full coverage of the sensor grid, we define $P \in ([0,1] \times [0,1])^{5\times 5}$ with $p_{i,j} = (x_{i,j}, y_{i,j}) = \frac{1}{4} \cdot (j,i)$ (See Figure 7.2).

Definition: *Estimated Positions (Relative)*

ESTIMATED POSITIONS (RELATIVE):
To relate an estimated position to the corresponding measurement position, we denote the estimated positions as $\tilde{P}_{d_S,h} \in (\mathbb{Q} \times \mathbb{Q})^{5x5}$ with $\tilde{p}_{d_S,h,i,j} = (\tilde{x}_{d_S,h,i,j}, \tilde{y}_{d_S,h,i,j})$ for sensor spacing d_S and height h.

The algorithms receive inputs with attenuated noise component.

To counteract noise for every sensor during position estimation, we calculate the arithmetic mean $\bar{\mathbf{B}}_{i,j}$ based on a hundred magnetic field measurements, yielding four average magnetic field strengths $\overline{m}_{i,j} = \|\bar{\mathbf{B}}_{i,j}\|_2$. The position estimation algorithms receive the sensor positions $S = (s_{i,j})$ and the averaged values $\overline{m}_{i,j}$ as input.

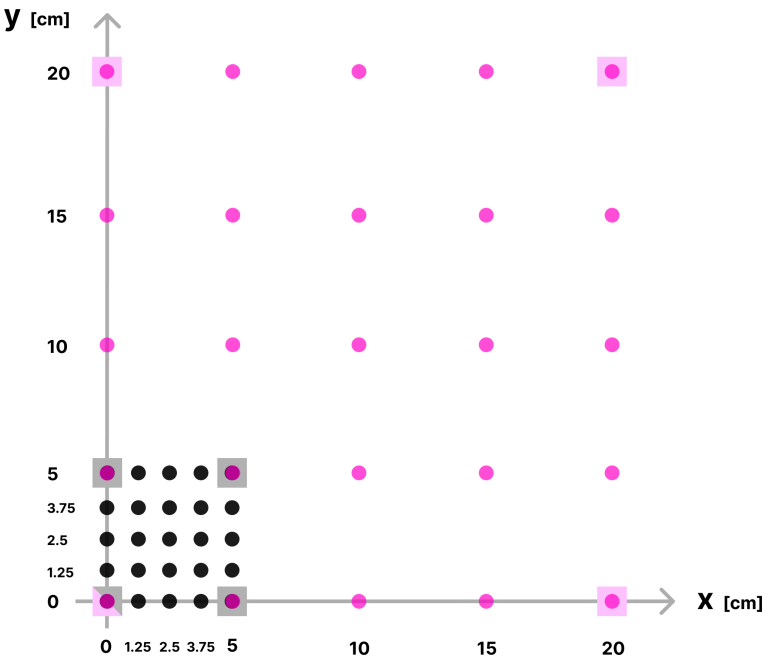

Figure 7.1: The measurement positions for sensor spacing d_S = 5cm (black points, gray sensors) and for d_S = 20cm (pink points, light pink sensors).

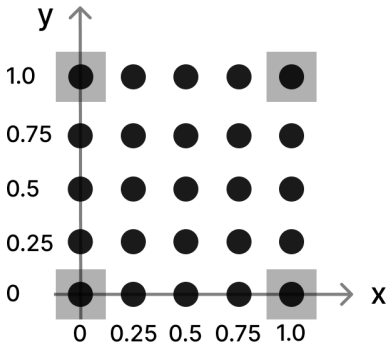

Figure 7.2: The relative sensor and the measurement positions.

7.2 Position Estimation Algorithms

Moving forward, we introduce two 2D position estimation approaches.

The first approach is based on a linear weighting algorithm (See Algorithm 1). However, as explained in Section 2.1, the magnetic field decreases with the inverse cube of the

The first 2D position estimation approach is based on linear weighting.

distance. Since we apply a linear weighting algorithm to non-linear values, the estimated points will likely be distorted.

The second approach linearizes the measurements before applying linear weighting.

Therefore, as a second approach, we linearize the values beforehand by $v_i' = \sqrt[3]{\frac{1}{v_i}}$ (See Algorithm 2). This inverse operation reverses the order of magnitude, resulting in a mirrored estimated position $\tilde{p} = (\tilde{x}, \tilde{y})$ along the center of the measurement positions. We mirror $\tilde{p}$ again by $\tilde{p} = (1 - \tilde{x}, 1 - \tilde{y})$.

As the first approach is based on raw values, we refer to it as "Raw-Alg". Respectively, we refer to the second approach, that is based on linearized values, as "Lin-Alg".

Algorithm 1: Raw-Alg: 2D Position Estimation by Linear Weighting of Raw Values

input: Sensor positions $S = (s_{i,j})$ and the values $v_{i,j}$ for each sensor

output: estimated point $\tilde{p}$

$\tilde{p} \leftarrow \frac{\sum_{i=0}^{3} s_{i,j} \cdot v_{i,j}}{\sum_{i=0}^{3} v_{i,j}}$;

return $\tilde{p}$;

7.3 Comparing the Shape of the Estimated Positions to the Measurement Positions

As mentioned previously, it is irrelevant whether the estimated positions are close to the real magnet positions, as long as the estimated positions $\tilde{P}$ appropriately reflect the input gesture. That should be the case, when the shape of P is preserved in $\tilde{P}$. Before we can compare their shapes, we need to introduce a metric to compare $\tilde{P}$ with P:

Algorithm 2: Lin-Alg: 2D Position Estimation by Linear Weighting of Linearized Values

input: Sensor positions $S = (s_{i,j})$ and values $v_{i,j}$ for each sensor

output: estimated point $\tilde{p}$

$v_{i,j} \leftarrow \sqrt[3]{(\frac{1}{v_{i,j}})}$;

$\tilde{p} \leftarrow$ Raw-Alg$(S, (v_{i,j}))$

return $\tilde{p} = (1 - \tilde{x}, 1 - \tilde{y})$;

TOTAL ESTIMATION ERROR (TEE):

$$E_{total}(\tilde{P}) = \sum_{i=0}^{4}\sum_{j=0}^{4} \|p_{i,j} - \tilde{p}_{i,j}\|_2 \tag{7.1}$$

where $\tilde{P} \in (\mathbb{Q} \times \mathbb{Q})^{5x5}$ is a matrix of estimated positions.

Definition: *Total estimation error (TEE)*

The TEE is not invariant of shape-preserving operations like translation and scaling. In order to compare the shape of P and $\tilde{P}$, we use the TEE to introduce a translation and scaling invariant metric, which transforms $\tilde{P}$ in order to minimize E_{total}. To do that, we introduce translation and scaling operations of $\tilde{P}$.

The TEE alone is not enough to compare the shapes of $\tilde{P}$ and P.

$$translate(\tilde{P}, t) = \tilde{P} + (t \cdot \mathbb{J}) \tag{7.2}$$

where $\tilde{P} \in (\mathbb{Q} \times \mathbb{Q})^{5x5}$ is a matrix of estimated positions,
$\mathbb{J} \in (\mathbb{Q} \times \mathbb{Q})^{5x5}$ is a matrix full of ones,
$t \in (\mathbb{Q} \times \mathbb{Q})$ translates each element of $\tilde{P}$.

$$scale(\tilde{P}, \gamma) = (\tilde{P} - P_{center}) \cdot \gamma + P_{center} \tag{7.3}$$

where $\tilde{P} \in (\mathbb{Q} \times \mathbb{Q})^{5x5}$ is a matrix of estimated positions,
$\gamma \in \mathbb{Q}$ scales the estimated positions,
$P_{center} = (0.5, 0.5) \cdot \mathbb{J} \in (\mathbb{Q} \times \mathbb{Q})^{5x5}$ contains the center of P

in each entry.

Based on these operations, we can introduce a metric that compares the shape of P and $\tilde{P}$ by correcting the differences between P and $\tilde{P}$ in regards of translation and scaling:

Definition: *Shape deviation error (SDE)*

SHAPE DEVIATION ERROR (SDE):

$$E_{shape}(\tilde{P}) = \min_{\substack{t \in (\mathbb{Q} \times \mathbb{Q}) \\ \gamma \in \mathbb{Q}}} E_{total}(scale(translate(\tilde{P}, t),\ \gamma)) \tag{7.4}$$

where $\tilde{P} \in (\mathbb{Q} \times \mathbb{Q})^{5x5}$ is a matrix of estimated positions.

Chapter 8

Discussion

Moving forward, we discuss the evaluation results in regard to the estimated positions, the scaled estimated positions, the scalings and the performance of the position estimation algorithms. Then, we review the requirements that we set for our system in Chapter 4 and compare our approach to related work.

8.1 Discussion of Evaluation Results

8.1.1 Estimated Positions

In the following we focus on the estimated positions, that emerged from the application of Raw-Alg (See Algorithm 1) and Lin-Alg (See Algorithm 2). The estimated positions are illustrated in the Figures B.1, B.2, B.3 and B.4.

The estimated positions increasingly centralize with the measurement height and increasingly spread with the sensor spacing.

When comparing the estimated positions for a fixed sensor spacing, it is salient that the estimated positions increasingly centralize with the measurement height. This is probably due to the fact that the respective magnet-sensor distances differ the most when the magnet is close to the sensor positions, resulting in larger differences in magnetic field measurements. Since the applied algorithms are based on linear weighting, more similar sensor measurements

lead to more central estimated positions. Another observation is that the estimated positions spread with increasing sensor spacing, which can be explained in the same manner.

8.1.2 Scaled Estimated Positions

The scaled estimated positions are illustrated in the Figures B.5, B.6, B.7 and B.8. All of them seem to be symmetric, so we can assume that the sensor measurements do not differ greatly.

Observations for Raw-Alg

Raw-Alg yields distorted estimated positions at larger sensor spacings and at smaller heights.

For the scaled estimated positions of Raw-Alg, we observe that the edges are often curved inwards. We suspect that the curvature is due to the cubically decreasing magnetic field (See Section 2.1). It is prominent that the curvature increases with the sensor spacing, but decreases with the height over the sensor grid. We suspect that it is the most prevalent at a small height, because there, the gradient of the magnetic field is the steepest, so its non-linear progression is picked up by the sensors and affects the results of a linear-weighting algorithm the most. Since the gradient of the magnetic field becomes more shallow with the distance (See Figure A.3), it can be more accurately approximated by a linear function with increasing distance. Thus, estimated positions can reproduce the shape of the measurement positions better and the curvature decreases. Another observation is that the curvature increases with the sensor spacing, which can be explained similarly.

Observations for Lin-Alg

For the scaled estimated positions based on Lin-Alg, we observe that the edges tend to be curved outwards, with the curvature decreasing with increasing sensor spacing.

This can be seen most easily by comparing the scaled estimated positions for the height h = 5cm of the different sensor spacings (excluding 15cm sensor spacing). Similar to the scaled estimated positions of Raw-Alg, the curvature decreases with increasing height. We suspect that the outwards curvature comes from a rounding of the corner positions. This rounding probably emerges from the fact that, when the magnet hovers over one corner at a specific sensor, the other sensors still sense the magnet to a significant extend. This results in their measured magnetic field being far from zero, dragging the estimated position more towards the center.

Lin-Alg yields inversely distorted estimated positions in comparison to Raw-Alg. Similarly, the distortion increases with larger sensor spacings and at smaller heights.

This explanation fits the observation that the corner rounding decreases with increasing sensor spacing and height, since a larger magnet-sensor distance leads to a weaker applied magnetic field at the other sensors.

8.1.3 Comparison of Scalings

As can be observed in Figure B.9, it seems that the optimal scaling γ for the scaled estimated positions of Raw-Alg and Lin-Alg can be described by a monotonically increasing function for each sensor spacing $d_S \in \{5, 10, 15, 20\}$. For each applied algorithm respectively, the scaling at a fixed height decreases with increasing sensor spacing. When comparing the scaling progression of the algorithms for the same sensor spacing d_S, the similarity is very apparent and the corresponding scalings only seems to differ by a constant (See Figure B.9 bottom).

The scalings for the estimated positions of Raw-Alg and Lin-Alg only differ by a factor.

8.1.4 Algorithms

In the following, we use the shape deviation error E_{shape} as a performance indicator, since a smaller value should correspond to a more accurately reproduced shape of the measurement grid and a larger value indicates a higher deviation from it.

	Sensor Spacing				
Height	**5cm**	**10cm**	**15cm**	**20cm**	**Sum**
5cm	1.775	2.015	3.464	2.727	9.981
10cm	0.457	1.032	1.686	2.093	5.268
15cm	0.879	0.868	1.084	1.416	4.247
20cm	3.069	1.530	1.923	1.966	8.488
Sum	6.180	5.445	8.157	8.202	27.984

Table 8.1: Based on **Raw-Alg (Algorithm1)**, this table summarizes the shape deviation error $E_{shape}(\tilde{P}_{d_S,h})$ of the estimated positions $\tilde{P}_{d_S,h},\ d_S, h \in \{5, 10, 15, 20\}$. For each sensor spacing, we marked the smallest error and biggest error across all heights.

	Sensor Spacing				
Height	**5cm**	**10cm**	**15cm**	**20cm**	**Sum**
5cm	1.259	1.039	4.373	1.160	7.831
10cm	0.500	0.809	1.409	1.391	4.109
15cm	0.939	0.910	1.188	1.399	4.436
20cm	2.986	1.611	2.012	2.906	9.605
Sum	5.683	4.369	8.983	6.856	25.981

Table 8.2: Based on **Lin-Alg (Algorithm2)**, this table summarizes the shape deviation error $E_{shape}(\tilde{P}_{d_S,h})$ of the estimated positions $\tilde{P}_{d_S,h},\ d_S, h \in \{5, 10, 15, 20\}$. For each sensor spacing, we marked the smallest error and biggest error across all heights.

	Sensor Spacing				
Height	**5cm**	**10cm**	**15cm**	**20cm**	**Sum**
5cm	0.516	0.976	-0.909	1.567	2.150
10cm	-0.043	0.223	0.277	0.702	1.159
15cm	-0.060	-0.042	-0.104	0.017	-0.189
20cm	0.083	-0.081	-0.089	-0.940	-1.117
Sum	0.497	1.076	-0.826	1.346	2.003

Table 8.3: Based on Table 8.1 and Table 8.2, this table subtracts the SDE of Lin-Alg from the SDE of Raw-Alg for the corresponding entries. Hence, the entry is positive if Raw-Alg yielded a larger SDE and vice versa.

Performance of Raw-Alg

Raw-Alg overall performs best at 10cm sensor spacing and worst at 20cm sensor spacing.

The following observations, see Table 8.1. Taking all sensor spacings into account, Raw-Alg overall performed the worst close to the sensor grid at $h = 5$ and the best at $h = 15$. An exception to this pattern are the scaled estimated positions with 5cm sensor spacing, where the algorithm yields the best SDE at $h = 10$ and the largest at $h = 20$. When comparing the performance of Raw-Alg for each sensor spacing, Raw-Alg predominantly performed the best at $d_S = 10$ and worst at $d_S = 20$. However, the data sets $\tilde{P}_{15,5}$, $\tilde{P}_{20,10}$ and $\tilde{P}_{20,20}$ suffered from severe outliers, so a larger SDE is to be expected. Nonetheless, when considering the visualizations, Raw-Alg indeed seems to reproduce the shape of the measurement positions most accurately at 10cm sensor spacing (See Figure B.6).

Performance of Lin-Alg

Lin-Alg overall performs best at 10cm sensor spacing and worst at 15cm sensor spacing.

The following observations are based on the data in Table 8.2. Unlike Raw-Alg, Lin-Alg primarily shows the smallest SDE at $h = 20$ across all sensor spacings. However, as mentioned earlier, the estimated positions $\tilde{P}_{15,5}$ suffered from a severe outlier, so under optimal conditions, $E_{shape}(\tilde{P}_{15,5})$ might be smaller than $E_{shape}(\tilde{P}_{15,20})$. Like Raw-Alg, Lin-Alg overall yielded the smallest SDE at 10cm sensor spacing.

Comparing the Performance of Raw-Alg and Lin-Alg

Lin-Alg overall yields a better performance than Raw-Alg.

Table 8.3 shows that Lin-Alg yields performed better for sensor spacings of 5cm, 10cm and 20cm compared to Raw-Alg, while Raw-Alg performed better at 15cm sensor spacing. Moreover, while Lin-Alg predominantly yielded a smaller sum SDEs in 5cm and 10cm height over all sensor spacings, Raw-Alg did so in 20cm height. Their overall performance is similar at 15cm sensor spacing. It is prominent that their largest difference in performance is in 5cm height. The difference sinks up to around 15cm height and grows

again up to 20cm height. There does not seem to be a pattern in regard to the sensor spacings.

All in all, the results show that, out of the sensor spacings and algorithms tested, our setup works most accurately at 10cm sensor spacing using algorithm Lin-Alg. However, note that this statement only holds when using the ∅8mmx2mm disk magnet. When using another magnet, a different sensor spacing might be more favorable.

Algorithm Limitations

Magnet movements may be detected that do not occur in reality.

As mentioned earlier, the area on which the estimated positions are reproduced increasingly centralizes with the height. This might impair gesture recognition using Lin-Alg, because people alter the height of their hands while performing gestures. For example, when starting a gesture at $h = 10$ and lowering the hand to $h = 5$, the estimated positions would indicate a hand movement to the edges of the positions, even though the 2D position of the hand has not changed in reality. Therefore, using another position estimation algorithm could be more favorable.

8.2 Checking the Established Requirements

In Chapter 4, we specified the requirements for our system:

(1) Expandable sensing area

(2) Overdrive distance $h_{min} \leq$ 2cm

(3) Feasible 2D position estimation of the magnet up to $h_{max} \geq$ 30cm

(1) We made the sensing area of our setup expandable by designing a modular sensor adapter PCB in Chapter 5.2. However, adaptations in hardware and software still need

to be made in order to support a seamlessly extendable sensing area.

(2) In Chapter 6, we chose the ∅8mmx2mm disk magnet with an overdrive distance of 2cm.

(3) According to the evaluation results, 2D position estimation of the magnet is feasible up to 15-20cm, using Lin-Alg and 10cm sensor spacing.

All in all, we met most of the established requirements. Still, some work needs to be done in order to fulfill them completely.

8.3 Comparison to Other Approaches

In contrast to other approaches, our approach allows for gestural input in mid-air.

Our system supports a larger reliable input distance than other magnet-based approaches designed for gestural input. FingerPad (Chan et al. [2013]) only supports an effect sensing range of 2.1cm from the sensor plate. Liang et al. [2013] reported a maximal input distance of 44mm across all their papers. uTrack by Chen et al. [2013] supports a volume of 19.2cm^3 ($\pm$ 80mm around the x-axis, $\pm$ 60mm around the y-axis and 0-80mm at the z-axis). On the other hand, the approach of Hu et al. [2010] works at a larger distance from the sensors compared to our approach: They support distances of 5cm-45cm with magnets as small as ∅4mmx5mm. However, their system is not designed for gesture recognition. Lastly, the infrared-based approach by Gong et al. [2017] supports sensing distances between 0.5cm and 30cm, but their gestures are limited to micro thump-tip gestures.

Other approaches allow for 3D position estimation.

Furthermore, while our approach is limited to 2D gesture recognition, Chen et al. [2013] supports 3D gesture recognition using only two 3-axis Hall sensors. Similarly, Hu et al. [2010] is able to accurately estimate the 3D position of a magnet.

Other gesture recognition approaches like Fingerpad (Chan et al. [2013]), uTrack (Chen et al. [2013]), Cyclops (Chan

Our approach is more convenient to be used on a daily basis.

et al. [2015]), LightRing (Kienzle and Hinckley [2014]), the electrode armband by Zhang et al. [2016], the MMG based armband by Yamakawa and Nojima [2012] and Pyro (Gong et al. [2017]), proposed a powered hand-held device. In contrast, only our sensor grid needs to be powered and a hand-held input device for our system only needs to embed a magnet, meaning that it can be smaller and lighter with no heat generation. In our case, the input magnet can just be embedded into a daily object like a ring or a bracelet, which are both socially acceptable in terms of appearance and do not obstruct daily routines. Such an object can be easily put on and off, while other magnet-based gesture recognition approaches like Chan et al. [2013] and Chen et al. [2013] require a more careful installation on finger nails. The placement on the finger nail(s) also restricts the user from carrying out daily routines when wearing these devices. All in all, these reasons make our setup more comfortable to users compared to the other approaches.

Other gesture recognition approaches support mobile applications, while ours does not.

In return, these self-powered devices are suitable for mobile applications and some even for environmental interaction (Chan et al. [2015]), while our setup can only be used locally. This also means that several sensor grids are needed for different applications. On the other hand, the locality makes tailored applications possible, e.g. for specific rooms or objects. An example would be a desk, where the sensor grid can be embedded on the tabletop's bottom and by that, extend a computer's functionality or replace other devices like a computer mouse. Another example is a couch in the living room, into which the sensor grid can be embedded in order to replace the TV remote, control the room lighting or adjust the TV's volume.

The sensor calibration of our system is frail and needs to be automated in the future.

Similar to GaussSense (Liang et al. [2012]), a current disadvantage of our system is the frail calibration. When the sensors are moved in space, the surrounding magnetic field changes and the calibration is invalid. This may significantly impair the performance of an applied position estimation algorithm. Our current calibration also restricts our setup from being embedded into frequently moved objects like doors, but this could be solved by automatically calibrating the sensor grid from time to time. In contrast, FingerPad (Chan et al. [2013]) and uTrack (Chen et al. [2013])

on the other hand do not calibrate the sensors, since the device-wearing hand is moved all the time. Because their reliable input range is significantly smaller than ours, their devices might still work without calibration, because the magnet is significantly closer to the sensors and therefore the signal-to-noise ratio might be significantly higher.

Similar to Liang et al. [2015], our approach is constructed in a way that allows for an extendable sensing area. A direct comparison of our system to other approaches in terms of performance is not possible, since the gesture recognition rate of our system has not been examined yet.

Chapter 9

Summary and Future Work

9.1 Summary and Contributions

Our system consists of a sensor grid out of four AMR sensors that is suitable for 2D mid-air gesture recognition in combination with a ∅8mmx2mm disk magnet.

In this thesis, we constructed a modular AMR sensor grid that is suitable for 2D mid-air gesture recognition. In order to achieve this, we firstly considered AMR sensor characteristics and chose a sensor that can reliably detect weak magnetic fields. Then, we constructed a modular sensor adapter PCB that allows for an extendable sensing area in the future, where we took care to keep the PCB-induced magnetic field as low as possible. Moreover, we implemented sensor communication and sensor calibration with an Arduino. Furthermore, we investigated the anisotropy of the sensor in case that it affects position estimation results significantly. After that, we conducted experiments with various magnets to find one that is suitable for mid-air interaction without overdriving the sensors in potential applications. Based on the results, we chose a ∅8mmx2mm disk magnet and determined the maximal sensor spacing for this magnet to be around 20cm.

Lastly, we examined the suitability of our system for 2D gesture recognition. For that, we constructed a 2x2 sensor grid and took measurements on an aligned 5x5 mea-

The position estimation algorithm that linearizes the measurements beforehand and then applies linear weighting performed the best at 10cm sensor spacing.

surement grid for different sensor spacings and heights. Then, we applied two algorithms on the same data, where both algorithms are based on linear weighting. Thereby, the first algorithm gets the raw values as input and the second algorithm linearizes the raw values before applying linear weighting. We evaluated the resulting estimated grids based on the quality of the reproduced measurement grid shape. We compared the results of both algorithms and came to the conclusion that the shape of the measurement grid was the best reproduced by the algorithm based on the linearized values at a sensor spacing of 10cm.

9.2 Future Work

2D gesture recognition algorithms and user satisfaction should be evaluated on our system.

In the future, the performance of a 2D gesture recognizer (e.g. the $1 recognizer) should could be evaluated on our system in combination with the ∅8mmx2mm disk magnet, 10cm sensor spacing and Algorithm 2. Moreover, it should be investigated if users are satisfied with the user input height of 15-20cm that the ∅8mmx2mm disk magnet yields.

Applying other position estimation algorithms could be beneficial.

However, as we mentioned earlier, problems may arise in practice when using Algorithm 2, since it reports different 2D positions when the magnet height is changed. In that case, other position estimation algorithms should be evaluated on our hardware. A promising position estimation algorithm was provided by uTrack (Chen et al. [2013]). It could be applied to our system and could either enhance the functionality of the system to 3D gesture recognition or the estimated 3D position could be projected onto 2D space. Other approaches based on machine-learning tackle problems of all kinds, so it could be used on our system for position estimation or for the gesture recognition itself.

In addition, the sensing area of our approach should be made easily expandable, similar to Liang et al. [2015]. To achieve that and to facilitate hardware construction, I3C communication with the sensor could be implemented.

The evaluation results feature some outliers in regards of estimated positions. Thus, future work should find a solu-

tion to prevent or deal with outliers.

Lastly, the functionality of our approach could be extended, such that it is usable as a smart home control device, as proposed by Meier et al. [2019].

Appendix A

Magnet Experiment Results

Figures A.1, A.2 and A.3 show the results of the magnet experiments that we described in Chapter 6.

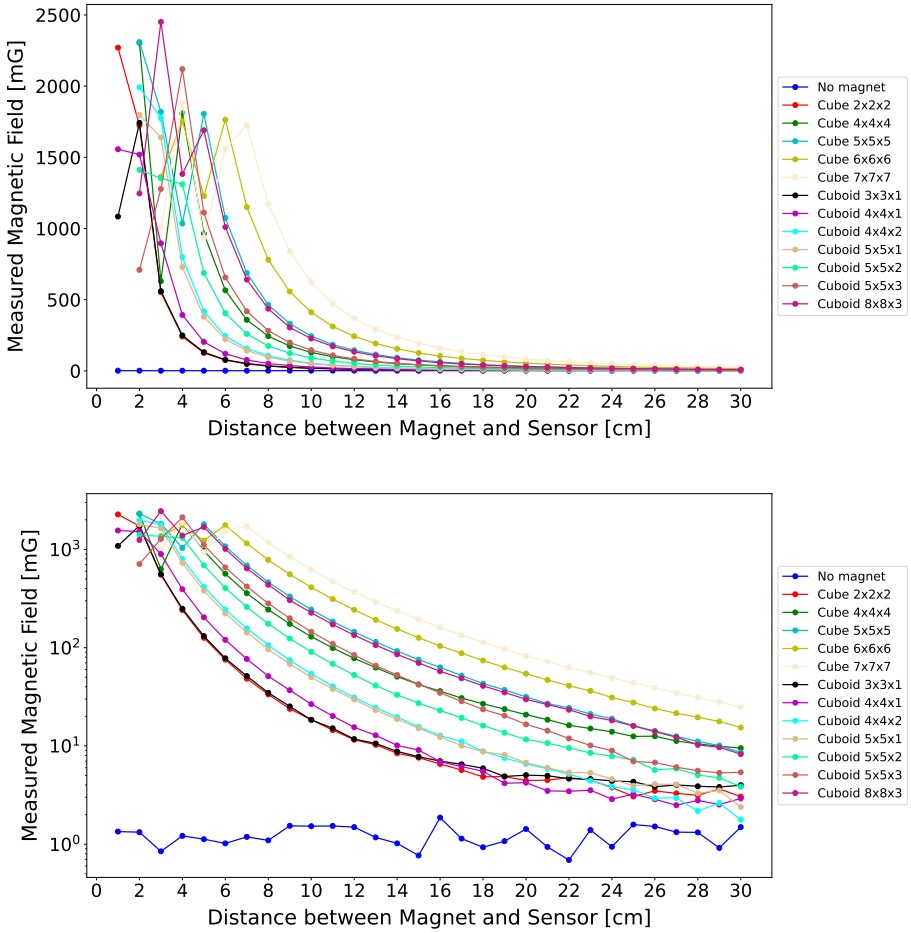

Figure A.1: The magnetic field measurements of the **cuboid magnets** taken centimeter by centimeter starting from the individual magnet's overdrive distance up to 30cm from the sensor. The upper figure has a linear y-axis, giving away the overall shape of the measurement curves. The lower figure has a logarithmic y-axis, such that values close to zero can be differentiated better. The legend gives the type and dimension of each magnet. For more information on the magnets, see Table 6.1.

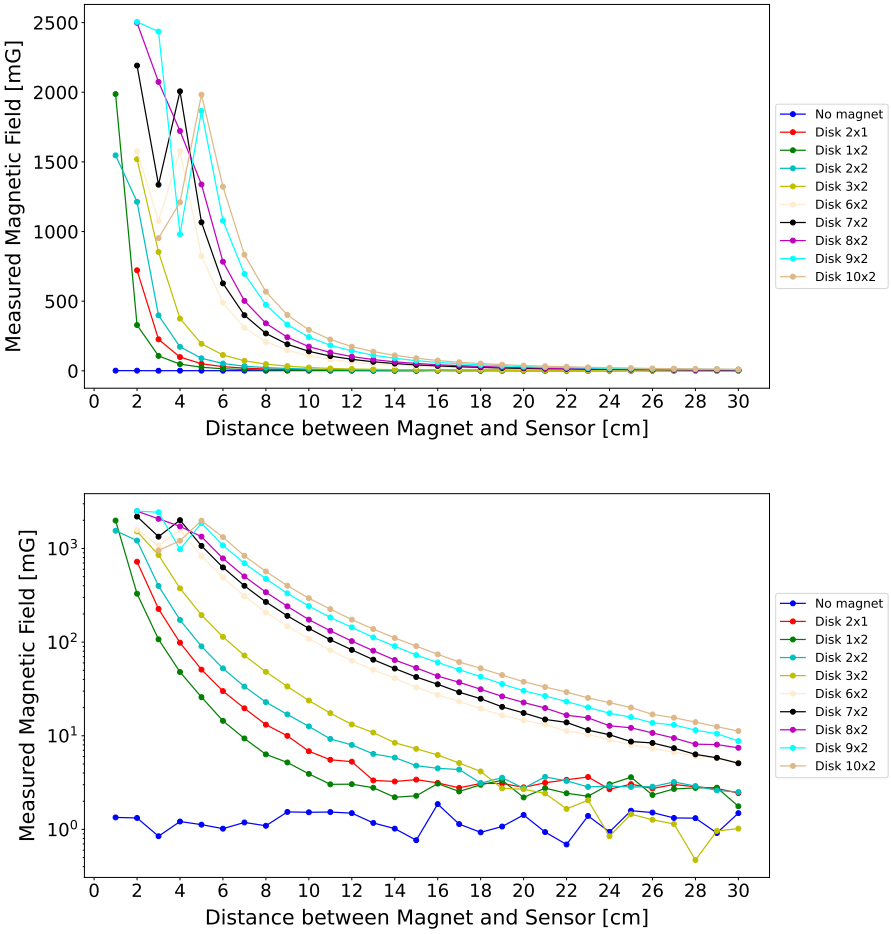

Figure A.2: The magnetic field measurements of the **disk magnets** taken centimeter by centimeter starting from the individual magnet's overdrive distance up to 30cm from the sensor. The upper figure has a linear y-axis, giving away the overall shape of the measurement curves. The lower figure has a logarithmic y-axis, such that values close to zero can be differentiated better. The legend gives the type and dimension of each magnet. For more information on the magnets, see Table 6.1.

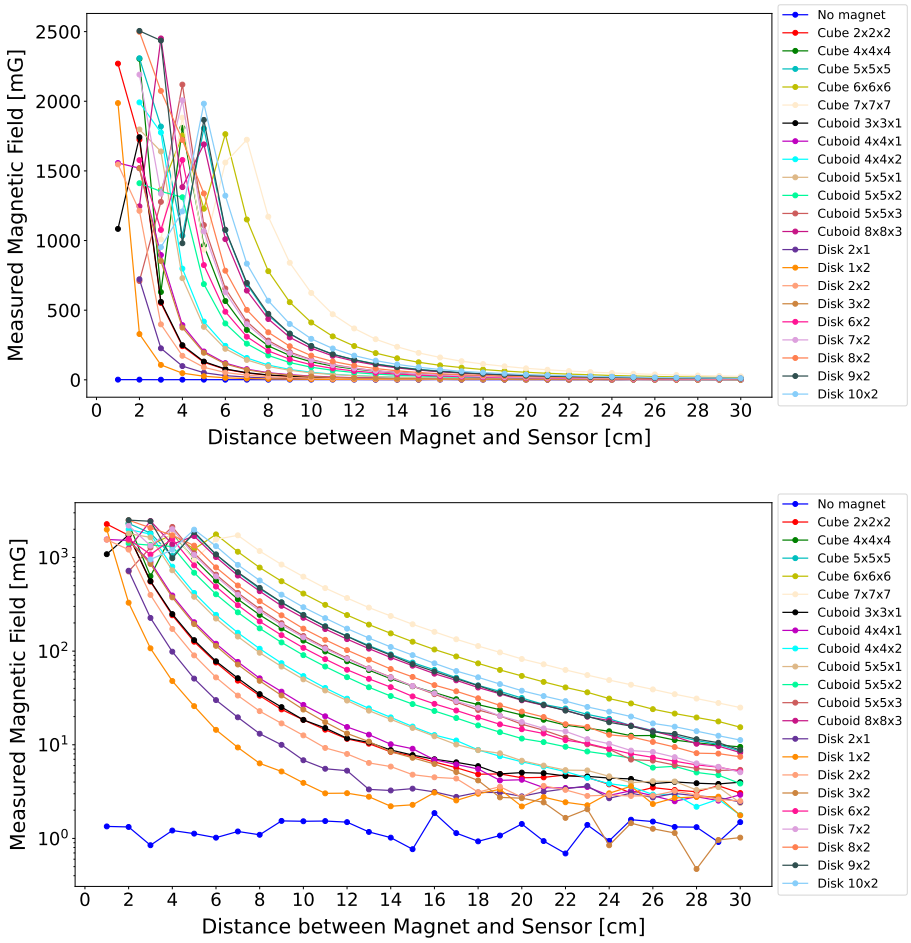

Figure A.3: The magnetic field measurements of **all magnets** taken centimeter by centimeter starting from the individual magnet's overdrive distance up to 30cm from the sensor. The upper figure has a linear y-axis, giving away the overall shape of the measurement curves. The lower figure has a logarithmic y-axis, such that values close to zero can be differentiated better. The legend gives the type and dimension of each magnet. For more information on the magnets, see Table 6.1.

Appendix B

Evaluation Results

The **estimated positions** of both algorithms are shown in Figure B.1 for sensor spacing d_S = 5cm, Figure B.2 for d_S = 10cm, Figure B.3 for d_S = 15cm and Figure B.4 for d_S = 20cm.

The **scaled estimated positions** are shown in Figure B.5 for d_S = 5cm, Figure B.6 for d_S = 10cm, Figure B.7 for d_S = 15cm and Figure B.8 for d_S = 20cm.

Figure B.9 shows a **comparison of the scalings**.

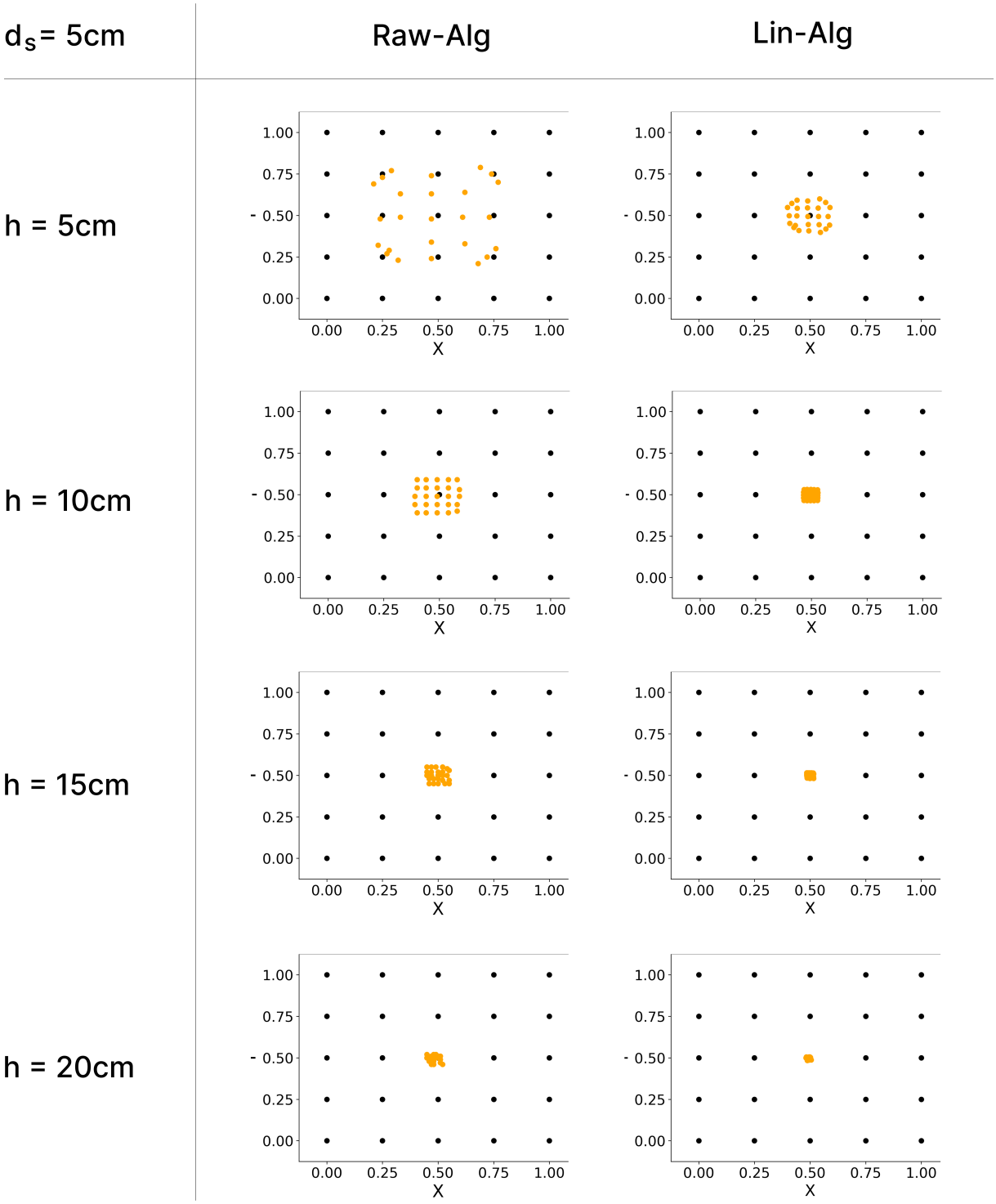

Figure B.1: The estimated positions (orange points) of Raw-Alg and Lin-Alg for **sensor spacing d_S = 5cm** and height $h \in \{5, 10, 15, 20\}$. The measurement positions are shown in black points.

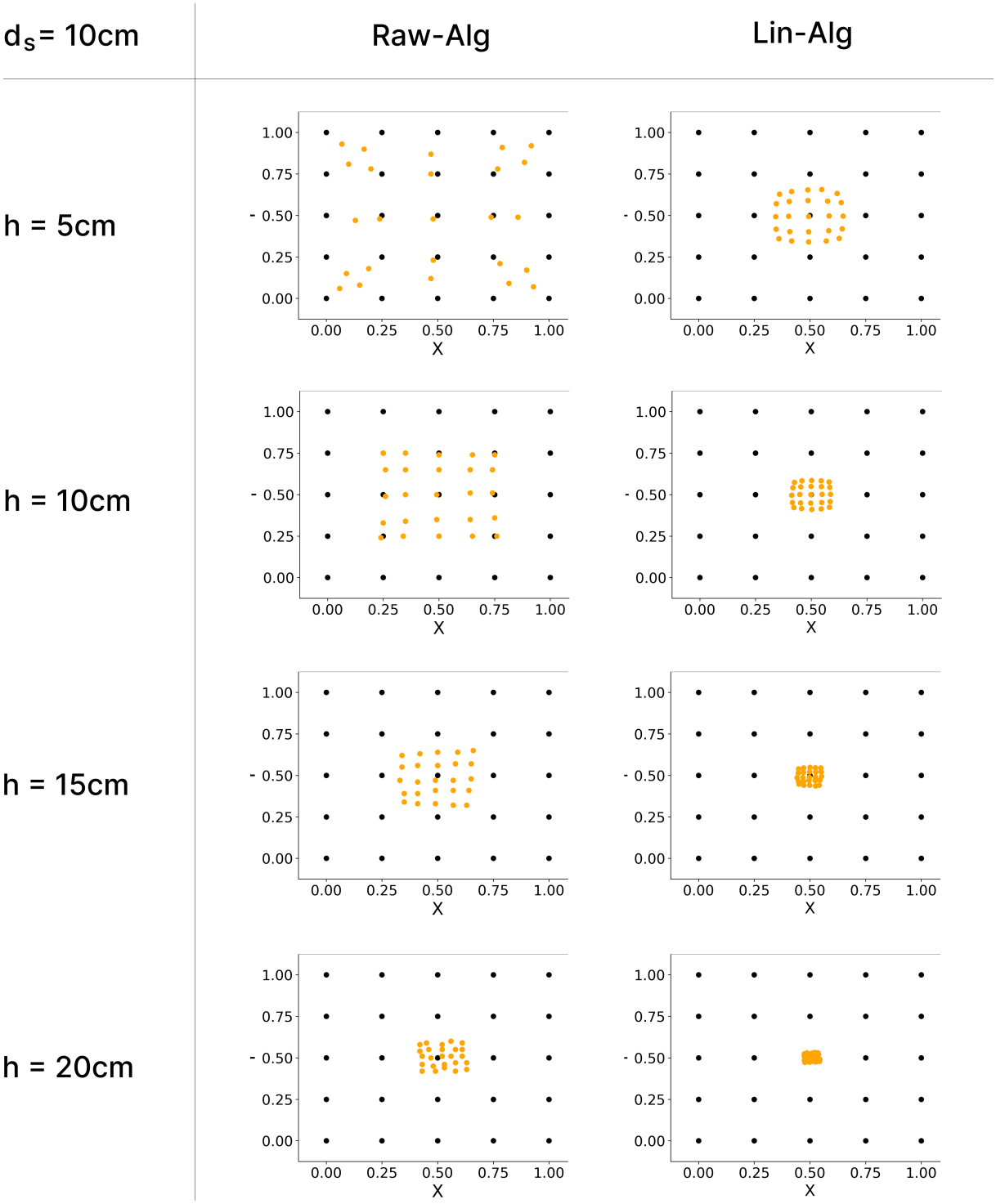

Figure B.2: The estimated positions (orange points) of Raw-Alg and Lin-Alg for **sensor spacing** d_S **= 10cm** and height $h \in \{5, 10, 15, 20\}$. The measurement positions are shown in black points.

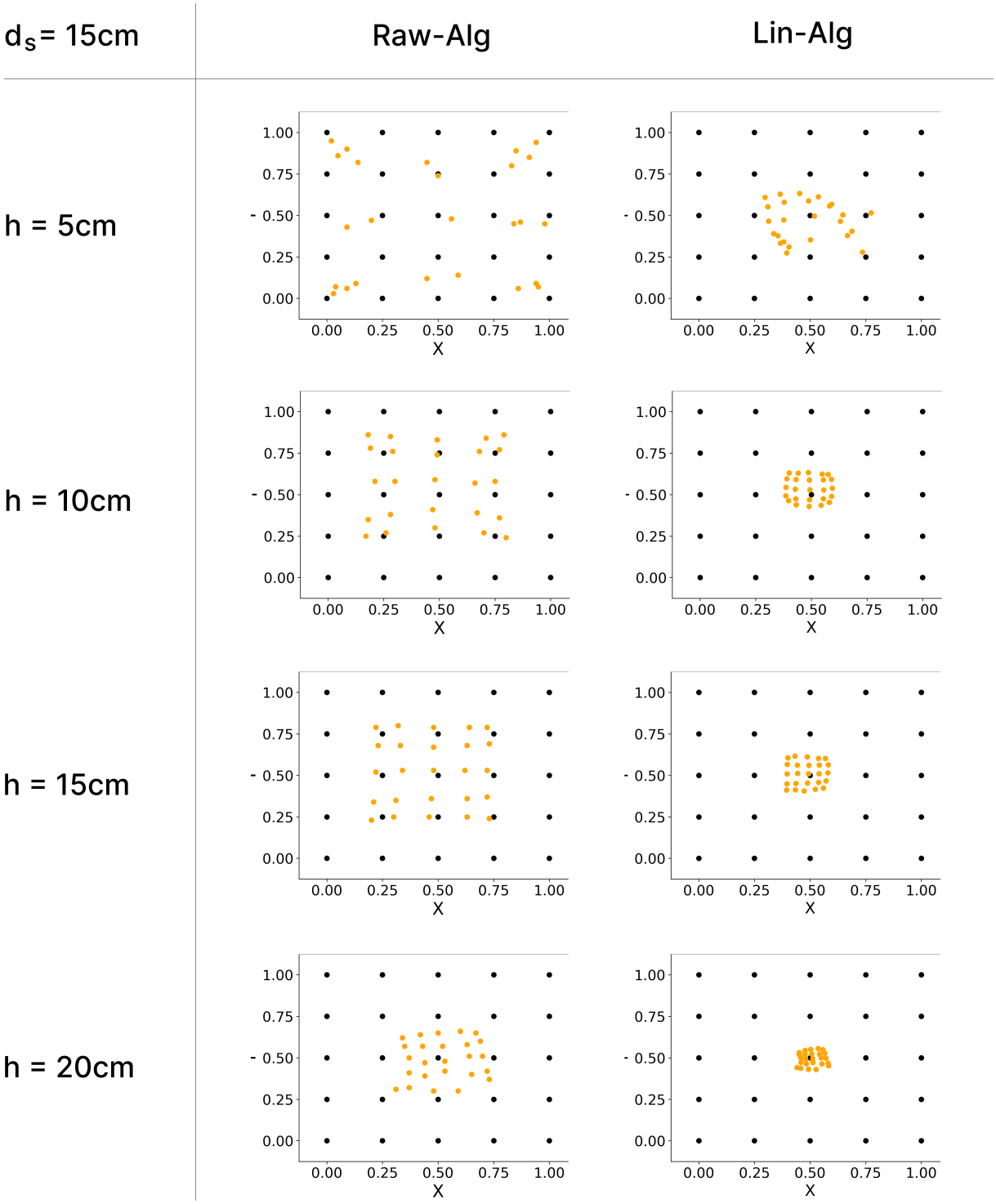

Figure B.3: The estimated positions (orange points) of Raw-Alg and Lin-Alg for **sensor spacing d_S = 15cm** and height $h \in \{5, 10, 15, 20\}$. The measurement positions are shown in black points.

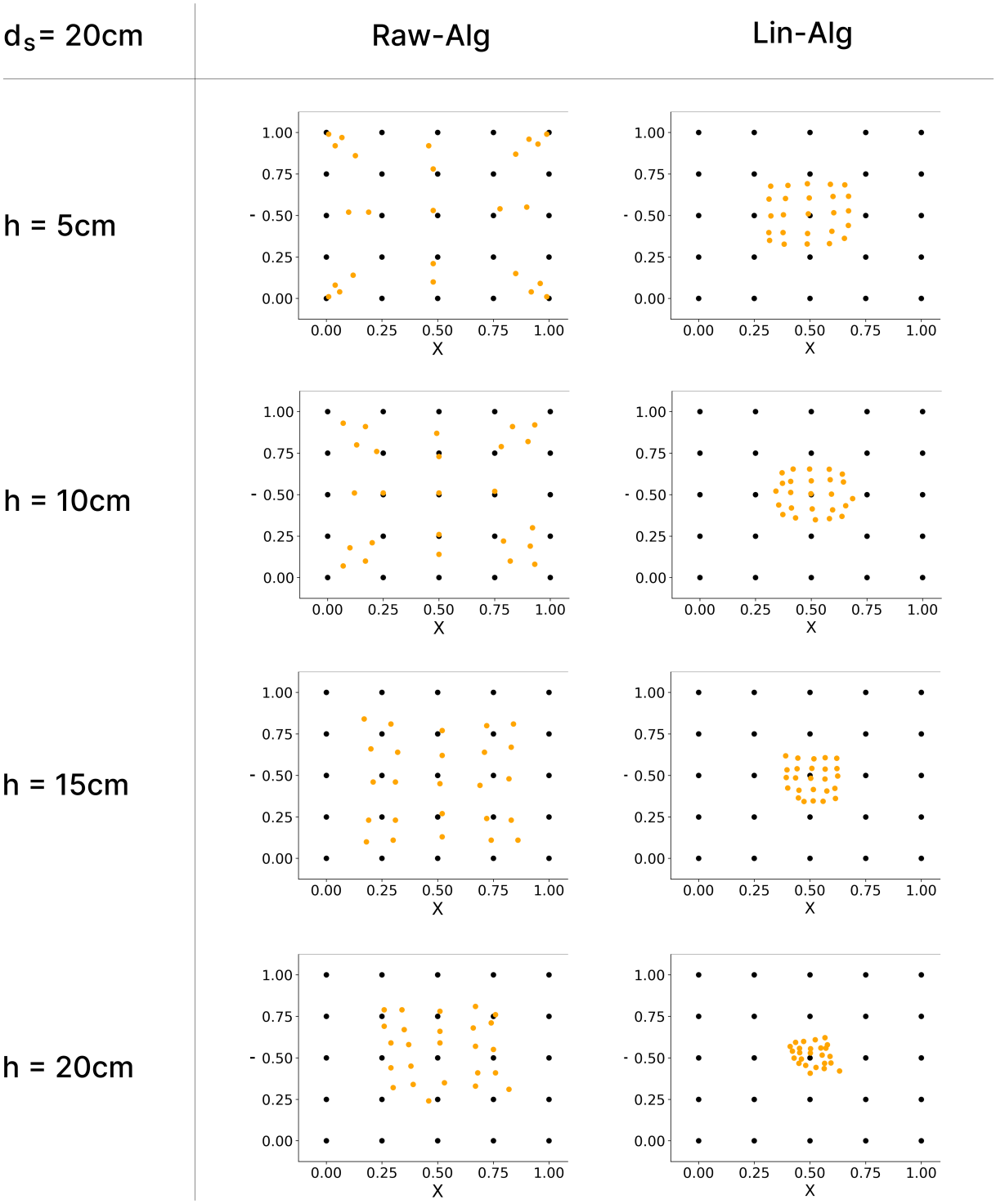

Figure B.4: The estimated positions (orange points) of Raw-Alg and Lin-Alg for **sensor spacing** d_S **= 20cm** and height $h \in \{5, 10, 15, 20\}$. The measurement positions are shown in black points.

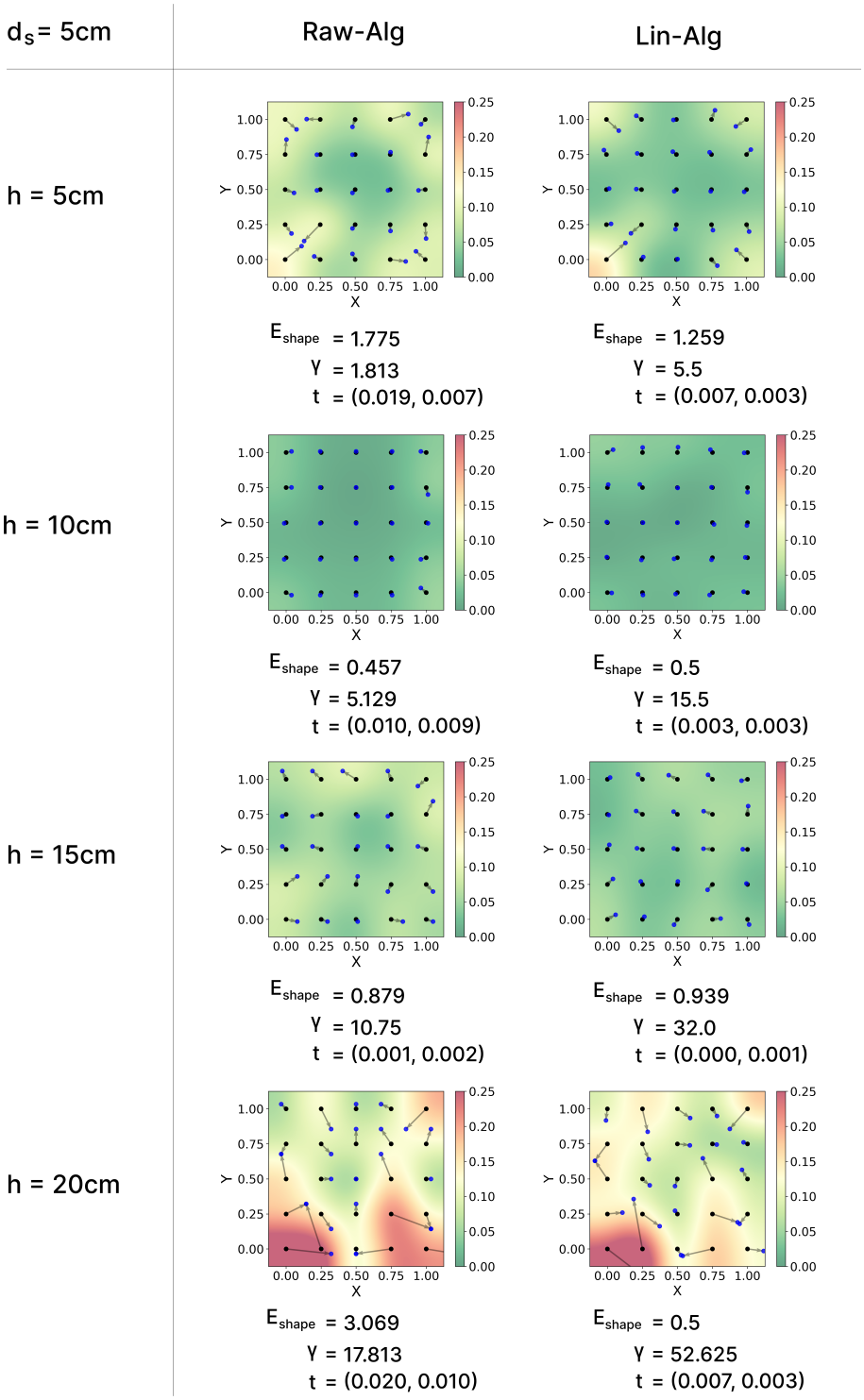

Figure B.5: The scaled estimated positions (blue points) for **sensor spacing d_S = 5cm**, height $h \in \{5, 10, 15, 20\}$, both for Raw-Alg and Lin-Alg. The measurement positions are shown in black points, where a 2D vector shows the error between a measurement point and an estimated point. The heat map visualizes the shape deviation error. See Section 7.3 for an explanation of the variables.

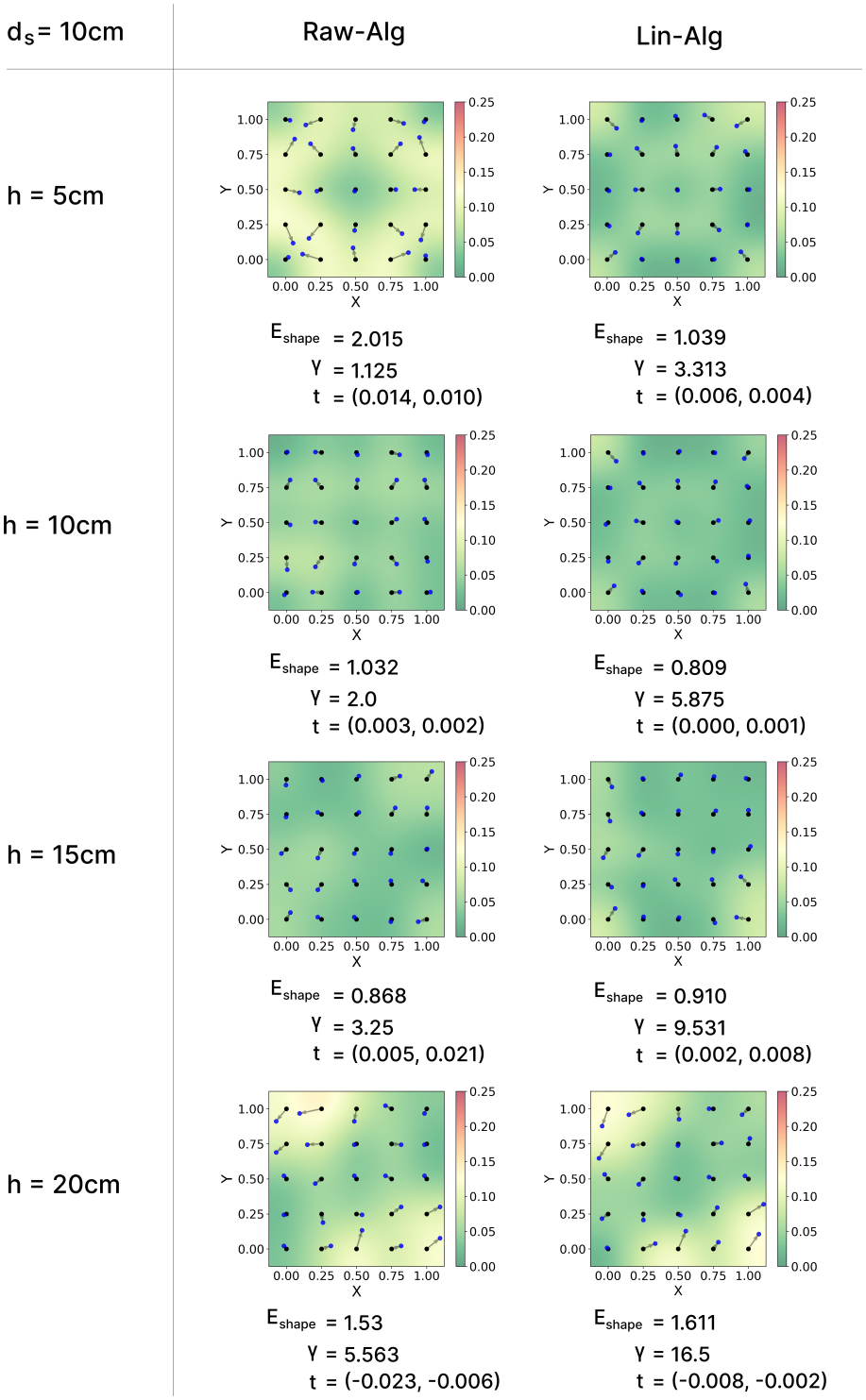

Figure B.6: The scaled estimated positions (blue points) for **sensor spacing d_S = 10cm**, height $h \in \{5, 10, 15, 20\}$, both for Raw-Alg and Lin-Alg. The measurement positions are shown in black points, where a 2D vector shows the error between a measurement point and an estimated point. The heat map visualizes the shape deviation error. See Section 7.3 for an explanation of the variables.

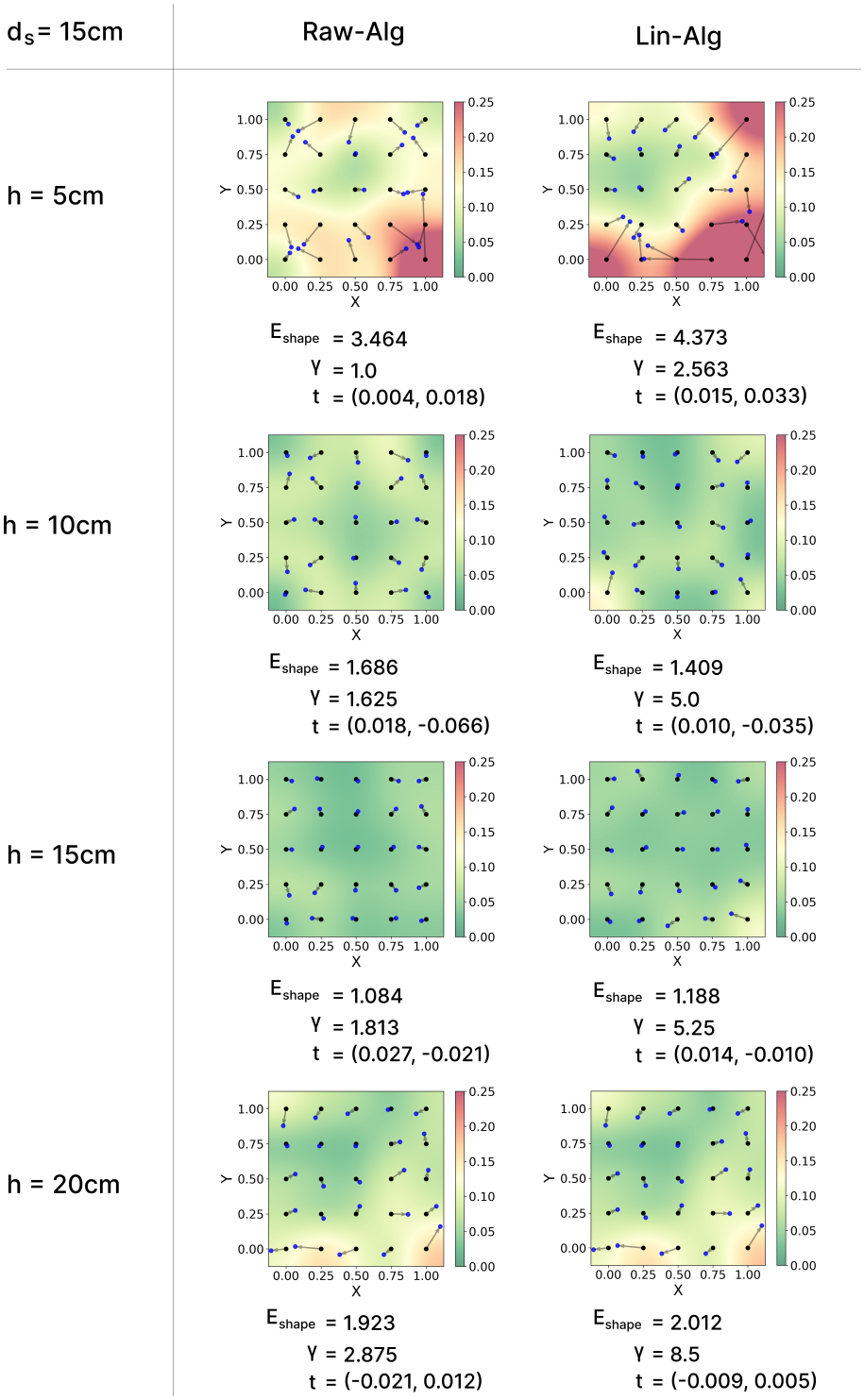

Figure B.7: The scaled estimated positions (blue points) for **sensor spacing d_S = 15cm**, height $h \in \{5, 10, 15, 20\}$, both for Raw-Alg and Lin-Alg. The measurement positions are shown in black points, where a 2D vector shows the error between a measurement point and an estimated point. The heat map visualizes the shape deviation error. See Section 7.3 for an explanation of the variables.

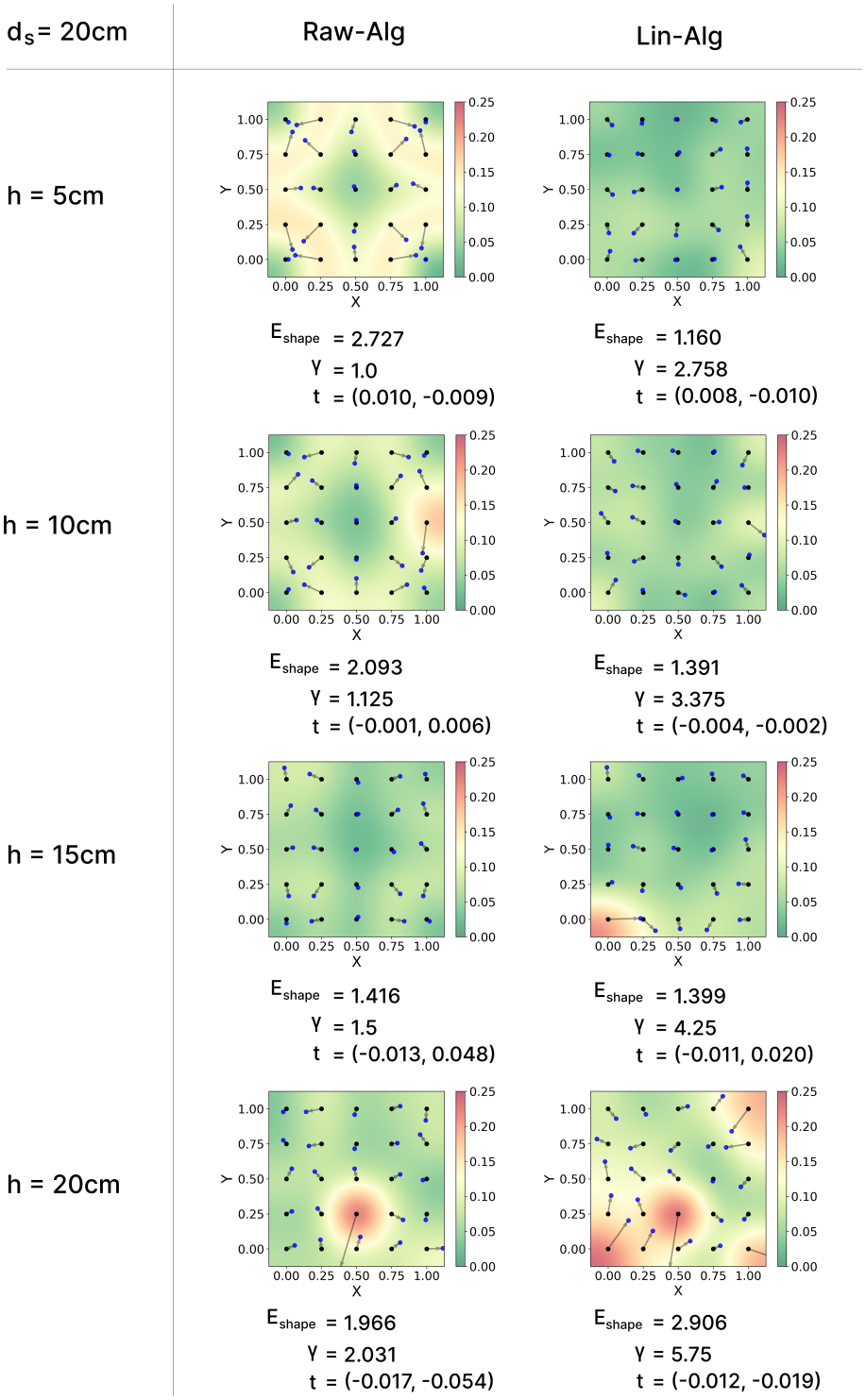

Figure B.8: The scaled estimated positions (blue points) for **sensor spacing** d_S **= 20cm**, height $h \in \{5, 10, 15, 20\}$, both for Raw-Alg and Lin-Alg. The measurement positions are shown in black points, where a 2D vector shows the error between a measurement point and an estimated point. The heat map visualizes the shape deviation error. See Section 7.3 for an explanation of the variables.

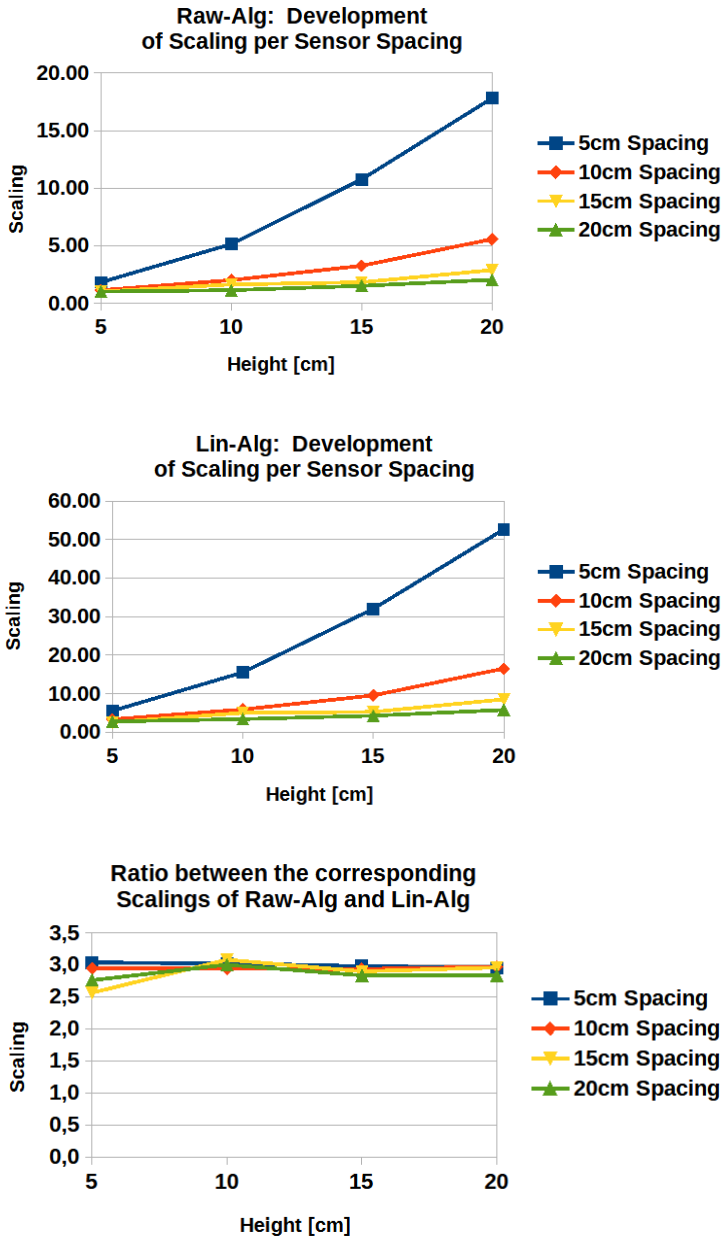

Figure B.9: The development of the optimal scaling γ per sensor spacing for Raw-Alg (See Algorithm 1) and Lin-Alg (See Algorithm 2). The Figure at the bottom shows the ratio between the corresponding scalings. See Section 7.3 for an explanation on γ.

Appendix C

Adapter PCB File, Software Files and Experiment Data

The following repository contains the MMC5603NJ sensor data sheet by Memsic, the adapter PCB file made in DesignSpark, all Arduino and Python files implemented for the experiments and all CSV files containing the experiment results.

https://git.rwth-aachen.de/i10/thesis-laura-drescher-manaa-amr-sensor-grid.git

Bibliography

Esmeralda Campos, Eder Hernandez, Pablo Barniol, and Genaro Zavala. Phenomenographic analysis and comparison of students' conceptual understanding of electric and magnetic fields and the principle of superposition. *Physical Review Physics Education Research*, 17(2):020117, 2021.

Liwei Chan, Rong-Hao Liang, Ming-Chang Tsai, Kai-Yin Cheng, Chao-Huai Su, Mike Y Chen, Wen-Huang Cheng, and Bing-Yu Chen. Fingerpad: private and subtle interaction using fingertips. In *Proceedings of the 26th annual ACM symposium on User interface software and technology*, pages 255–260, 2013.

Liwei Chan, Yi-Ling Chen, Chi-Hao Hsieh, Rong-Hao Liang, and Bing-Yu Chen. Cyclopsring: Enabling whole-hand and context-aware interactions through a fisheye ring. In *Proceedings of the 28th Annual ACM Symposium on User Interface Software & Technology*, pages 549–556, 2015.

Ke-Yu Chen, Kent Lyons, Sean White, and Shwetak Patel. utrack: 3d input using two magnetic sensors. In *Proceedings of the 26th annual ACM symposium on User interface software and technology*, pages 237–244, 2013.

Ke-Yu Chen, Shwetak N Patel, and Sean Keller. Finexus: Tracking precise motions of multiple fingertips using magnetic sensing. In *Proceedings of the 2016 CHI Conference on Human Factors in Computing Systems*, pages 1504–1514, 2016.

JMD Coey. Permanent magnet applications. *Journal of Magnetism and Magnetic Materials*, 248(3):441–456, 2002.

Woon Siong Gan. Quantum image processing. In *Quantum Acoustical Imaging*, pages 83–86. Springer, 2022.

Jun Gong, Yang Zhang, Xia Zhou, and Xing-Dong Yang. Pyro: Thumb-tip gesture recognition using pyroelectric infrared sensing. In *Proceedings of the 30th Annual ACM Symposium on User Interface Software and Technology*, pages 553–563, 2017.

Yizheng Gu, Chun Yu, Zhipeng Li, Weiqi Li, Shuchang Xu, Xiaoying Wei, and Yuanchun Shi. Accurate and low-latency sensing of touch contact on any surface with finger-worn imu sensor. In *Proceedings of the 32nd Annual ACM Symposium on User Interface Software and Technology*, pages 1059–1070, 2019.

Janne Haverinen and Anssi Kemppainen. Global indoor self-localization based on the ambient magnetic field. *Robotics and Autonomous Systems*, 57(10):1028–1035, 2009.

Jonathan Hook, Stuart Taylor, Alex Butler, Nicolas Villar, and Shahram Izadi. A reconfigurable ferromagnetic input device. In *Proceedings of the 22nd annual ACM symposium on User interface software and technology*, pages 51–54, 2009.

Chao Hu, Mao Li, Shuang Song, Rui Zhang, Max Q-H Meng, et al. A cubic 3-axis magnetic sensor array for wirelessly tracking magnet position and orientation. *IEEE Sensors Journal*, 10(5):903–913, 2010.

Mike Jackson. Anisotropy of magnetic remanence: a brief review of mineralogical sources, physical origins, and geological applications, and comparison with susceptibility anisotropy. *Pure and Applied Geophysics*, 136(1):1–28, 1991.

Wolf Kienzle and Ken Hinckley. Lightring: always-available 2d input on any surface. In *Proceedings of the 27th annual ACM symposium on User interface software and technology*, pages 157–160, 2014.

Rong-Hao Liang, Kai-Yin Cheng, Chao-Huai Su, Chien-Ting Weng, Bing-Yu Chen, and De-Nian Yang. Gausssense: Attachable stylus sensing using magnetic sensor grid. In *Proceedings of the 25th annual ACM symposium on User interface software and technology*, pages 319–326, 2012.

Rong-Hao Liang, Kai-Yin Cheng, Liwei Chan, Chuan-Xhyuan Peng, Mike Y Chen, Rung-Huei Liang, De-Nian Yang, and Bing-Yu Chen. Gaussbits: magnetic tangible bits for portable and occlusion-free near-surface interactions. In *Proceedings of the SIGCHI Conference on Human Factors in Computing Systems*, pages 1391–1400, 2013.

Rong-Hao Liang, Han-Chih Kuo, and Bing-Yu Chen. Gaussstarter: Prototyping analog hall-sensor grids with breadboards. In *Adjunct Proceedings of the 28th Annual ACM Symposium on User Interface Software & Technology*, pages 49–50, 2015.

Howard C Lovatt and Peter A Watterson. Energy stored in permanent magnets. *IEEE transactions on magnetics*, 35(1): 505–507, 1999.

Teruo Matsushita. *Electricity and magnetism*. Springer, 2014.

Phil Meier, Kris Rohrmann, Oussama Ferhi, Marvin Sandner, and Marcus Prochaska. A magnetic field sensor array as an universal smart home control device. In *2019 IEEE 8th Global Conference on Consumer Electronics (GCCE)*, pages 1055–1057. IEEE, 2019.

Xiongfei Meng and Resve Saleh. An improved active decoupling capacitor for "hot-spot" supply noise reduction in asic designs. *IEEE Journal of Solid-State Circuits*, 44(2): 584–593, 2009.

André Michaud. On the magnetostatic inverse cube law and magnetic monopoles. *International Journal of Engineering Research and Development e-ISSN*, pages 50–66, 2013.

Masa Ogata, Yuta Sugiura, Hirotaka Osawa, and Michita Imai. iring: intelligent ring using infrared reflection. In *Proceedings of the 25th annual ACM symposium on User interface software and technology*, pages 131–136, 2012.

Alfred Brian Pippard. *Magnetoresistance in metals*, volume 2. Cambridge university press, 1989.

RS Popovic, PM Drljaca, and C Schott. Bridging the gap between amr, gmr, and hall magnetic sensors. In *2002*

23rd International Conference on Microelectronics. Proceedings (Cat. No. 02TH8595), volume 1, pages 55–58. IEEE, 2002.

Marcus Rickert. *Funktionelle Normwerte und Einflussfaktoren an Unterarm und Hand gesunder männlicher Erwachsener*. PhD thesis, lmu, 2010.

Pavel Ripka and Michal Janosek. Advances in magnetic field sensors. *IEEE Sensors journal*, 10(6):1108–1116, 2010.

Casto Rivadulla, Guglielmo Foffani, and Antonio Oliviero. Magnetic field strength and reproducibility of neodymium magnets useful for transcranial static magnetic field stimulation of the human cortex. *Neuromodulation: Technology at the Neural interface*, 17(5): 438–442, 2014.

V Schlageter, P-A Besse, RS Popovic, and P Kucera. Tracking system with five degrees of freedom using a 2d-array of hall sensors and a permanent magnet. *Sensors and Actuators A: Physical*, 92(1-3):37–42, 2001.

John C Teel. Understanding noise in linear regulators. *Texas Instruments Analog Applicant*, 2005.

Slawomir Tumanski. Modern magnetic field sensors–a review. *Organ*, 10(1):1–12, 2013.

Radu-Daniel Vatavu and Laura-Bianca Bilius. Gesturing: A web-based tool for designing gesture input with rings, ring-like, and ring-ready devices. In *The 34th Annual ACM Symposium on User Interface Software and Technology*, pages 710–723, 2021.

Shuo Wang, Fred C Lee, and Willem Gerhardus Odendaal. Cancellation of capacitor parasitic parameters for noise reduction application. *IEEE Transactions on power electronics*, 21(4):1125–1132, 2006.

Martin Weik. *Computer science and communications dictionary*. Springer Science & Business Media, 2000.

Jacob O Wobbrock, Andrew D Wilson, and Yang Li. Gestures without libraries, toolkits or training: a $1 recognizer for user interface prototypes. In *Proceedings of the 20th annual ACM symposium on User interface software and technology*, pages 159–168, 2007.

Shumpei Yamakawa and Takuya Nojima. A proposal for a mmg-based hand gesture recognition method. In *Adjunct proceedings of the 25th annual ACM symposium on User interface software and technology*, pages 89–90, 2012.

Yang Zhang, Robert Xiao, and Chris Harrison. Advancing hand gesture recognition with high resolution electrical impedance tomography. In *Proceedings of the 29th Annual Symposium on User Interface Software and Technology*, pages 843–850, 2016.

Index

Typeset September 5, 2022